

Enhancing Variational Quantum Eigensolvers for SU(2) Lattice Gauge Theory via Systematic State Preparation

Klaus Liegener,¹ Dominik Mattern,² Alexander Korobov,³ Lisa Krüger,^{1,2} Manuel Geiger,³ Malay Singh,¹ Longxiang Huang,¹ Christian Schneider,^{1,2} Federico Roy,^{1,4} and Stefan Filipp^{1,2,5}

¹*Walther-Meissner-Institute, Walther-Meissner-Strasse 8, 85748 Garching, Germany*

²*Technical University of Munich, TUM School of Natural Sciences,*

Department of Physics, 85748 Garching, Germany

³*Technical University of Munich, TUM School of CIT,*

Department of Computer Science, 85748 Garching, Germany

⁴*Institute for Quantum Computing Analytics (PGI-12),*

Forschungszentrum Jülich, 52425 Jülich, Germany

⁵*Munich Center for Quantum Science and Technology (MCQST), 80799 Munich, Germany*

(Dated: March 5, 2026)

Computing the vacuum and energy spectrum in non-Abelian, interacting lattice gauge theories remains an open challenge, in part because approximating the continuum limit requires large lattices and huge Hilbert spaces. To address this difficulty with near-term quantum computing devices, we adapt the variational quantum eigensolver to non-Abelian gauge theories. We outline scaling advantages when using a spin-network basis to simulate the gauge-invariant Hilbert space and develop a systematic state preparation ansatz that creates gauge-invariant excitations while alleviating the barren plateau problem. We illustrate our method in the context of SU(2) Yang-Mills theory by testing it on a minimal toy model consisting of a single vertex in 3+1 dimensions. In this toy model, simulations allow us to investigate the impact of noise expected in current quantum devices.

I. INTRODUCTION

One of the most prominent open questions in modern quantum field theories is the mass gap problem [1]. In essence, it asks whether the energy gap between the vacuum (i.e., ground state) and the first excited state remains finite in the continuum limit for interacting theories in $d = 3$ (spatial) dimensions. Although progress has been made for some toy models [2–4], in general, numerically approximating the ground state and its energy remains computationally demanding, especially on large lattices. Simulations of *lattice gauge theories* (LGT) [5, 6] have steadily advanced in recent decades through the development of tools such as tensor network methods [7, 8]. However, as these methods break down for highly entangled states in dimensions $d \geq 2$, new computational approaches are required.

A promising pathway is quantum simulation on quantum computers [9–11]. Exploiting the exponential growth of the Hilbert space with qubit count has already proven successful in investigating Abelian gauge theories such as \mathbb{Z}_2 [12–14] and U(1) [15–17]. However, less progress has been made for non-Abelian gauge theories in $d \geq 2$, despite their physical relevance. This is mainly because the tools established for simulating Abelian theories often do not generalize to the non-Abelian setting. For example, when dealing with \mathbb{Z}_2 , the vacuum in the strong coupling limit can be prepared with a mean-field ansatz even at large scales [18]. In the non-Abelian setting, however, this ansatz fails due to the bosonic nature of the quantum numbers on each edge, see Figure 1 (a). First works on quantum simulations of SU(2) LGT have focused on truncating the theory to two energy levels per edge [19–21], i.e., making it \mathbb{Z}_2 -like, or simulating

the dynamics [22–24], often achieved by decomposing the Hamiltonian evolution into sequences of multi-qubit gates known as Trotter decomposition. The large number of required qubits and gates necessitates extremely low error rates, achievable only with future fault-tolerant quantum computers.

Today’s *noisy-intermediate scale quantum* (NISQ) computers instead rely on shallow algorithms, such as the *variational quantum eigensolver* (VQE) [25–27], in which the storage and preparation of the ground state on a quantum device are assisted by a classical optimization procedure. The built-in noise resilience of the VQE algorithm at the quantum level comes at the expense of unique challenges caused by sampling many irrelevant states, or the rapidly increasing number of measurements required to reach sufficient accuracy [28, 29]. Nonetheless, VQEs on available quantum hardware have already been used to generate accurate results for quantum chemistry with small- to medium-sized molecules [30] and in \mathbb{Z}_2 LGT [12]. The present manuscript demonstrates its viability for non-Abelian gauge theories as well.

A major challenge in non-Abelian gauge theories is the invariance under their local symmetry group described by the Gauss constraint, which renders most states unphysical. Common VQE ansätze, such as the *hardware-efficient ansatz* (HEA) (see Figure 1 (b)), which samples almost the full Hilbert space, are therefore ill-suited for scaling. Intuitively, this can be explained as follows: at each lattice vertex, the constraint eliminates a fraction $q > 1/2$ of the possible states. As the lattice size increases, i.e., the number of vertices N grows, the fraction of physical states among all possible states decreases as $(1-q)^N$. This implies an exponentially unfavorable scaling of HEA: too many irrelevant candidates render HEA

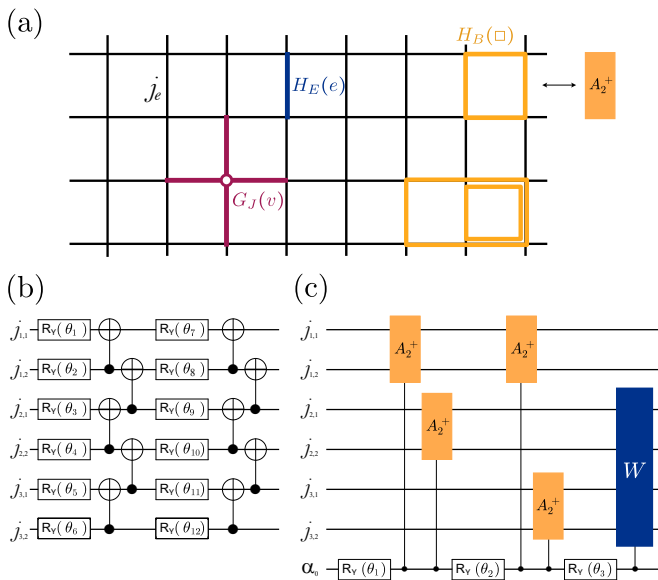


FIG. 1. (a) Schematic representation of an LGT system. A Gauss constraint G_J enforces physical relations between the quantum numbers j_e of edges e meeting at vertex v . The electric part H_E and the magnetic part H_B of the Kogut-Susskind Hamiltonian act on edges and plaquettes, respectively. Physical states may feature multiple excitations $j_e \in \mathbb{N}/2$ on the same edge and can be created by exciting various (potentially overlapping) plaquettes of the lattice. (b) The usual HEA enables short and dense gate layers but requires large optimization parameter count. (c) The physics-informed SSP ansatz preserves gauge-invariant excitations (shown for two-edge-plaquettes relevant for the toy model of Section III A), thereby reducing the optimization parameter count at the expense of more complicated controlled multi-qubit gates.

impractical for physically relevant lattice sizes.

To alleviate such scaling issues for the VQE in LGT, in this work we project out (most) unphysical states by expressing the ansatz on the gauge-invariant Hilbert space in the basis of spin-network functions [31–33]. This construction, coined *systematic state preparation* (SSP) ansatz, only generates gauge-invariant excitations – effectively excluding the remaining unphysical states. Its core idea is to only insert quantum gates which act on neighboring lattice sites in such a way that the Gauss constraint is preserved, see Figure 1 (c).

The paper is structured as follows: in Section II we recall the basics of $SU(2)$ Yang-Mills LGT. We discuss the VQE algorithm and its associated scaling challenges. To alleviate some of these challenges, we establish the SSP protocol. In Section III A, we test our framework on a toy model: a single vertex in three spatial dimensions ($d = 3$) with periodic boundary conditions, representing the quantization of the symmetry-restricted phase space with imposed translational invariance of classical Yang-Mills theory. Finally, in Section III B, we use the SSP to determine the vacuum of the toy model in both ideal and emulated noisy environments.

II. METHODS

A. LGT and spin-network representation

Given a $d \geq 2$ -dimensional lattice γ with spacing ϵ , the discretized dynamics of a Yang-Mills theory [34] is defined by the *Kogut-Susskind Hamiltonian* [35]

$$H = g_E \sum_e H_E(e) - g_B \sum_{\square} H_B(\square), \quad (1)$$

where the electric part H_E acts on the edges $e \in \gamma$ of the lattice and the magnetic part H_B on the plaquettes \square of γ , i.e., closed loops composed of four edges. See Section A for details. The system is characterized by its coupling parameters $g_E, g_B \geq 0$. The Hamiltonian is invariant under local $SU(2)$ transformations and, as a consequence, only states obeying this symmetry are physical. In the Hamiltonian formulation, this invariance is implemented through the *Gauss constraint*, which generates these local $SU(2)$ transformations and whose discretized version following Guillemin-Sternberg [36] reads:

$$G_J(v) = \sum_{e \cap v \neq \emptyset} P_J(e), \quad (2)$$

where v denotes lattice vertices, i.e., the initial and terminal points, $e(0)$ and $e(1)$, of all edges $e \in \gamma$. The operators P_J are the gauge-covariant fluxes, i.e., the conjugate variables of the holonomies h over the gauge field [37–39]. These operators act on the Hilbert space of $SU(2)$ -valued functions over the lattice, commonly referred to as the *kinematical Hilbert space*

$$\mathcal{H} = \otimes_{e \in \gamma} \mathcal{H}_e, \quad \mathcal{H}_e = L_2(SU(2), d\mu), \quad (3)$$

with $d\mu$ being the Haar measure over $SU(2)$. Section A provides an explicit representation of those operators. In the following, we restrict the kinematical Hilbert space to its physical subspace – the kernel of the Gauss constraint (2):

$$\mathcal{H}_G = \{\psi \in \mathcal{H} \mid G_J(v)|\psi\rangle = 0 \forall v \in \gamma\}. \quad (4)$$

This defines the gauge-invariant Hilbert space.

Several bases of \mathcal{H}_G have been proposed to make computing the ground state feasible, see e.g. [22, 40, 41]. Choosing the correct one is non-trivial, and the consensus has emerged that the most suitable basis often depends on the problem at hand. The following outlines why the spin-network basis is advantageous when having the goal to eventually perform simulations of LGTs on current NISQ-type quantum computers.

The spin-network basis for $SU(2)$ relies on the fact that the irreducible representations (irreps) of a compact Lie group form a complete basis for square-integrable functions on the group (according to the Peter&Weyl theorem [42]). For $SU(2)$, these irreps are given by the Wigner- D -functions, $D_{m_e n_e}^{j_e}$, which serve as natural building blocks for states on individual lattice edges [43], and are labeled by the quantum numbers $j_e \in \mathbb{N}/2$ (called spins)

and $m_e, n_e \in \{-j, \dots, j-1, j\}$ for each edge e of the lattice. The collection of labels over all edges is denoted by \vec{j} , i.e., $j_e \in \vec{j}$ for each edge e , and similarly for \vec{m}, \vec{n} . To enforce gauge invariance, at every vertex the m, n -labels of adjacent edges are contracted with SU(2)-invariant tensors called *intertwiners* $\iota^v \in \vec{\iota}$, where we again denote the collection of intertwiners for all vertices as $\vec{\iota}$. This gives rise to the spin-network functions [31–33]:

$$|T_{\vec{j}, \vec{\iota}}\rangle = \sum_{e_k \in \gamma} \sum_{\vec{m}, \vec{n}} (\otimes_{e \in \gamma} |D_{m_e n_e}^{j_e}\rangle) \quad (5)$$

$$\left(\prod_{v \in \gamma} \iota_{m_{e_1} \dots n_{e_6}}^v \delta_{e_1(0), v} \dots \delta_{e_6(1), v} \right) \in \mathcal{H}_{\mathcal{G}}.$$

Each spin-network function $T_{\vec{j}, \vec{\iota}}$ is fully determined by \vec{j} of irreps over all edges $e \in \gamma$ and the choice of intertwiners $\vec{\iota}$ on all vertices $v \in \gamma$.

For the cubic lattices considered in this work, vertices and their intertwiners are 6-valent. Without loss of generality, 6-valent intertwiners can be decomposed into multiple 3-valent intertwiners [44], also known as Wigner-3j-symbols. Those symbols store information about a triple of spins j meeting at the vertex and are denoted by [43]

$$\iota_{m_1, m_2, m_3} := \begin{pmatrix} j_1 & j_2 & j_3 \\ m_1 & m_2 & m_3 \end{pmatrix}. \quad (6)$$

An explicit construction of the decomposition is given in Section A. Not all triples of spins j yield non-zero gauge-invariant functions. In other words, the spin-network basis allows for the existence of residual states. These are non-physical states whose associated 3j-symbols automatically vanish unless the following conditions are satisfied [44]:

$$j_1 + j_2 + j_3 \in \mathbb{N}, \quad (7)$$

$$|j_1 - j_2| \leq j_3 \leq j_1 + j_2. \quad (8)$$

Each condition eliminates 1/2 of the possible combinations of SU(2) irreps at each 3-valent intertwiner. As a consequence, the fraction of physical states for N 3-valent intertwiners decreases as $1/4^N$. Therefore, even in the spin-network basis, randomly sampling the full Hilbert space to find a physical state scales unfavorably.

In summary, while this description of the gauge-invariant Hilbert space reduces a significant amount of complexity compared to simulating the full lattice Hilbert space, it still grows exponentially with lattice size but with a smaller prefactor. Finally, if one restricts to states satisfying (7) and (8), the prefactor reduces further.

B. VQE and its challenges

Projecting onto the spin-network basis allows a lattice to be simulated with fewer qubits than representing the full LGT Hilbert space. Because this reduction directly impacts near-term quantum simulations, we now describe

how to facilitate ground state preparation in this setting. Finding the ground state Ω of the Kogut-Susskind Hamiltonian H , i.e., solving

$$H|\Omega\rangle = E_0|\Omega\rangle \quad (9)$$

on a quantum device, can be achieved using the VQE algorithm [25–27]. A VQE ansatz $A(\vec{\theta})$ is parametrized by a set of variational parameters $\vec{\theta}$ chosen such that applying A on the digital ground state of a quantum computer, $|0\rangle$, explores a sufficiently large portion of the Hilbert space on which H is defined. If the ansatz is sufficiently expressive, Ω can be approximated, i.e.,

$$|\psi(\vec{\theta})\rangle := A(\vec{\theta})|0\rangle, \quad \text{s.t. } \exists \vec{\theta}^* : |\psi(\vec{\theta}^*)\rangle \approx |\Omega\rangle \quad (10)$$

VQEs have gained significant attention in the last decade due to their shallow circuit depth and variational nature leading to noise resilience. Despite these successes, VQEs face significant challenges, especially when scaling the system [28, 29]. In particular, the following main challenges can be identified: (i) required number of repeated measurements, (ii) availability of sufficiently many highly-coherent qubits, and (iii) the barren plateau problem for large optimization parameter landscapes. The remainder of this section provides a brief review of these items.

Challenge (i) is related to the exponential growth in the number of required measurements on the system with increasing dimension of H : the VQE determines $\vec{\theta}^*$ using the expectation value of the Hamiltonian as cost function, i.e.,

$$\min_{\vec{\theta}} \langle \psi(\vec{\theta}) | H | \psi(\vec{\theta}) \rangle \approx E_0, \quad (11)$$

which requires expressing the Hamiltonian in the set \mathcal{P}_{n_q} of all Pauli strings over n_q qubits, such that each string $P \in \mathcal{P}_{n_q}$ corresponds to a single measurement on the quantum device:

$$H = \sum_{\alpha} c_{\alpha} P_{\alpha}. \quad (12)$$

However, the number of possible qubit strings grows rapidly, $|\mathcal{P}_{n_q}| = 4^{n_q}$. If a Hamiltonian has support on all of them, its decomposition would demand a prohibitive number of measurements to obtain sufficient statistics and achieve a low-variance energy estimate. For example, in typical chemistry simulations the number of Pauli strings grows with $\mathcal{O}(n_q^4)$ [45].

The second challenge (ii) is the scaling of the number of qubits with increasing number of vertices N , which is driven by two factors: First, meaningful predictions require small discretization errors, i.e., large lattice sizes. Second, the Wigner functions $D_{mn}^{(j)}$ for SU(2) run over $j \in \mathbb{N}/2$, hence require infinitely many degrees of freedom to be fully captured. It is thus necessary to introduce a cut-off j_{max} to restrict the system to finitely many qubits. Then, the naive qubit count scales as $\mathcal{O}(N j_{max}^{3d})$.

Finally, (iii) arises from the trade-off between adding more variational parameters $\vec{\theta}$ (which increase the chance to maximize overlap of the prepared state with the exact ground state as expressed in (10) by sampling more of the Hilbert space) on the one hand and on the other maintaining efficient convergence towards θ^* (which becomes exponentially harder with increasing number of parameters, also known as the *barren plateau problem* [25, 46–48]). The scaling of optimization parameters is crucial in settings such as gauge theories, where irrelevant directions exist in the parameter landscape of $\vec{\theta}$ due to the unphysical states and gauge degeneracies inherent in \mathcal{H} . This challenge affects all circuits, particularly those featuring large parameter counts (e.g. HEAs), which are known to struggle with this trade-off. This represents one of the main challenges VQEs need to address.

C. Scaling prospects in LGT with SSP

To help alleviate the aforementioned challenges, we have designed a new ansatz, coined the *systematic state preparation* (SSP), for VQEs in non-Abelian LGT and validate its feasibility and accuracy. We summarize its guiding principles here and refer to Section B for all details:

SSP utilizes the bosonic nature of the irreps on each link $j \in \{0, 1/2, \dots, j_{max}\}$ combined with the fact that the Hamiltonian only excites closed loops on the lattice. Instead of exciting individual qubits, SSP only generates gauge-invariant excitations by simultaneously manipulating all qubits storing information along said loops. We develop such an ansatz A by utilizing ancilla qubits and more complicated multi-qubit gates, e.g. A^\pm for raising/lowering the quantum numbers j . Schematically, we present this in Figure 1 (c), where SSP acts only once per layer on a qubit register, each corresponding to a single irrep j . This effectively excludes all the remaining unphysical states and we will argue in the following how it alleviates scaling issues, especially in the context of LGTs.

First, the scaling of Pauli strings is mitigated by both locality and translational invariance of LGTs irrespective of the ansatz used. It was estimated in [45] that the number of strings grows roughly with $\mathcal{O}(N j_{max}^4)$ with j_{max} being an ad hoc cut-off of the L_2 -space over each edge to allow encodability using $\log_2(j_{max})$ qubits and N being the number of vertices. For a fixed j_{max} , we have $n_q \sim N \log_2(j_{max})$ and the Pauli string scaling is therefore much milder than in, e.g., chemistry. Furthermore, since $[H_E(e), H_E(e')] = 0$ for all e, e' , a single measurement of all qubits suffices to extract the electric part independent of the lattice size and needs only to be repeated with some measurement count $n_s = n_s(\delta)$ to reach precision δ . Second, $H_B(\square)$ is local, and if two plaquettes \square and \square' do not share an edge, they can be decomposed into Pauli strings and measured simultaneously. Hence, the total magnetic part $\sum_{\square} H_B(\square)$ can be decomposed into

$4d$ sets of plaquettes which are pairwise non-intersecting, so the number of required measurements on the quantum device only grows with $\mathcal{O}(j_{max}^4)$. Decoupling the required measurements from lattice size in this way provides a fundamental scaling advantage. However, it does not reduce the measurement count n_s per Pauli string required to reach precision δ , which in uniform allocations still scales with N , i.e., $n_s \geq N/\delta^2$ [49]. While improved approximations for the required measurement count already exist (e.g. [50]), an alternative approach exploits the symmetries of the vacuum in LGT. In particular, the Hamiltonian H (and hence Ω) is invariant under real-space translations $T : v \mapsto v + \epsilon$ that leave the lattice invariant. In other words, it suffices to perform measurements of $H_E(e_o)$ and $H_B(\square_o)$ at some predefined point on the lattice, given by e_o or \square_o , respectively. This drastically reduces the measurement count, such that it scales with $\mathcal{O}(1/\delta)$ only. However, it comes at the expense of requiring that the prepared states $\psi(\vec{\theta})$ are invariant under T . We can in principle achieve this additional condition by ending the SSP ansatz with a gate sequence that performs a *group-average* over all translations [51]. The number of operations for symmetrizing a state grows with $\mathcal{O}(N^d)$, thus, this procedure is viable only in the late NISQ/fault-tolerant era, where the measurement count becomes prohibitive but gate fidelities are sufficient to extend A in such a way.

Second, the scaling of required qubits with lattice size is alleviated by the fact that SSP projects the Hilbert space to the gauge-invariant space of spin-network functions. Restricting to this set, which is only slightly larger than \mathcal{H}_G , allows us to work with a tamer scaling in qubit count. For comparison, when using the basis defined by all Wigner- D -functions, $D_{m_e n_e}^{j_e}$, one would require a naive scaling in terms of qubit numbers of $n_q \sim n_q^{\mathcal{H}} := N(3d \log_2(d_{j_{max}}) + 2d)$ with $d_j := 2j + 1$. SSP uses explicitly spin-network functions, which carry only one irrep per link but introduce additional intertwiners on each vertex, supported on $\pi \in \{0, \dots, 2j_{max}\}$. This leads to an effective qubit count scaling as $n_q \sim n_q^{\mathcal{H}} - 3N \log_2(d_{j_{max}}) + 3$ for $d = 2, 3$, which saves qubit resources especially on large lattices, $N \gg 1$, or large cut-offs, $j_{max} \gg 1$. Using this basis, the quantum computer may also store states whose irrep combinations correspond to trivially vanishing spin-network functions, because they violate (7) and (8). Hence, our construction overestimates \mathcal{H}_G by a small number of states, however, it eliminates most unphysical states¹. Moreover, the remaining conditions enable easy-to-implement symmetry verification and postselection protocols that aid error mitigation, see Section E and Section III B.

¹ Recent tensor network approaches advocate the use of the *dressed-site basis* [52, 53]. Here, the remaining gauge conditions are on the edges instead of being at the vertices. The required qubit count scales as $n_q \sim (4d-3)/(3d)n_q^{\mathcal{H}} - (4d-3)$ for the same accuracy, which motivates us to focus on the spin-networks in this manuscript, where the regime $j_{max} > 1/2$ is targeted.

Finally, a main motivation of introducing the SSP ansatz is to counteract the barren plateau problem: Reducing to \mathcal{H}_G in itself alleviates this issue, and a further potential is leveraged by replacing the usual HEA with a physically inspired ansatz: SSP requires fewer optimization parameters at the expense of an increased number of 2-qubit gates per layer by a factor depending on $d_{j_{max}}$. Crucially, the number of optimization parameters scales as $\mathcal{O}(N)$ per layer instead of as $\mathcal{O}(Nj_{max})$, as is the case for the HEA. Given that barren plateau problems arise when gradients vanish exponentially fast with the number of optimization parameters [46, 54], this reduction provides a significant speed-up, as will be demonstrated in the next section.

III. SSP PERFORMANCE ON THE 6-VERTEX TOY MODEL

In this section, we test the SSP ansatz by applying it to a toy model of 3D Yang-Mills theory with $SU(2)$ gauge group, which can be analyzed with emulators of mid-scale quantum devices.

A. Model: 6-valent vertex

The model consists of a single vertex v with periodic boundary conditions. Conceptually, we interpret this as a homogeneous system in which translation-invariance has been imposed prior to quantization. Note that, on the classical level, imposing translational invariance does not affect the symmetry-restricted phase space and its dynamics [55]. Yet, the extension of this phenomenon to the quantum level is still under investigation.

In our case, given that Hamiltonian and ground state are both translation invariant, we can still capture some relevant properties of a full 3D LGT in this reduced setting, such as correlations between different spatial directions: As many contemporary works focus on 2D simulations, their findings could be impacted by the presence of correlations between all three dimensions as this model allows to investigate. Further, since it can be fully simulated classically, it allows us to benchmark the accuracy of the VQE results.

By imposing periodic boundary conditions on the incoming and outgoing edges of the vertex, we simplify the Hilbert space to three copies over $SU(2)$, one for each direction, labeled by irreps $j_k^\pm := j_k$, $k \in \{1, 2, 3\}$. Going to the gauge-invariant Hilbert space contracts the corresponding Wigner-D functions with an intertwiner $\iota^{v, \pi_+, \pi_o, \pi_-}$ as specified in Section A in equation (A6), characterized by the internal quantum numbers π_-, π_o, π_+ . We discretize the Hamiltonian on this graph as follows: $H_E(e)$ as in (1) acts on the unique edge for each direction. We note that $H_B(\square)$ stems from a discretization of the curvature of the connection at v . To approximate it fully, it suffices at each vertex to consider

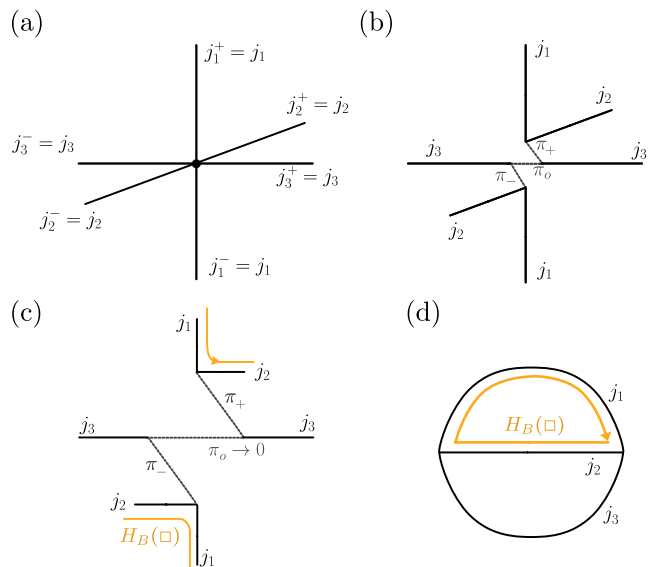


FIG. 2. Graphical representation of the toy model. (a) A single vertex in 3D with periodic boundary conditions, i.e., in- and outgoing irreps in each direction carry the same label. Projecting to the gauge-invariant Hilbert space is accomplished by choosing a basis of intertwiners (π_+, π_o, π_-) in (b). (c) We choose a discretization of the Hamiltonian approximating continuum Yang-Mills by attaching plaquettes such that π_o is not changed by action of H_B , hence separating the graph into superselection sectors. (d) Focusing on the sector $\pi_o = 0$ reduces the single-vertex graph to the Θ -graph.

only the plaquettes \square_{kl} oriented along pairs of positive outgoing edges j_k^+, j_l^+ . Due to the periodic boundaries, the minimal plaquettes encompass only two edges intersecting v and still approximate the curvature. This orientation choice simplifies the action of H as in the chosen basis for $\iota^{v, \pi_+, \pi_o, \pi_-}$, the label π_o remains invariant under the action of such a discretized H . Thus, the Hilbert space decomposes into superselection sectors with respect to the Hamiltonian, with each eigenvector supported in only one sector labeled by π_o . The ground state lies in the sector $\pi_o = 0$, which – due to the symmetries of the Wigner 3j-symbols – enforces $\pi_\pm = j_3^\pm$. In summary, this superselection sector of \mathcal{H} is entirely characterized by j_1, j_2, j_3 and hence becomes isomorphic to the Hilbert space over a Θ -graph, see Figure 2. See Section A for further details.

We stress that the Hilbert space over this finite lattice is still infinite dimensional ($j_k \in \mathbb{N}/2 \forall k$) and for it to be stored on a quantum device with finite qubit count, a cut-off j_{max} is required. This implies an unavoidable error in the full model, which requires careful analysis to be faithfully estimated. Yet, while recently proposed methods estimate this error for Abelian gauge groups [56], none have been extended to the non-Abelian setting so far. In this specific model, we can use the error introduced by cut-off j_{max} to gauge the accuracy of the VQE results, as deviations of the energy estimates below said error are no longer physically relevant. In other words, we

benchmark the effectiveness of the proposed SSP ansatz by how closely its energy estimates fall within the uncertainty margin introduced by the finite cut-off. This is particularly relevant in the strongly correlated regime, where the ground state no longer factorizes over the edges but is driven by non-local entanglement.

B. Simulated Implementation

To demonstrate that the SSP ansatz accurately estimates energy and identifies distinct phases of spatial correlation, we simulate its implementation.

The configuration space of coupling constants is described by the open set $g_E, g_B \geq 0$, which we compactify to a finite closed interval: Since any quantum system is invariant under a total reparametrization of the energy, only the total ratio between both couplings is physically relevant.² Hence, we express both in terms of a single parameter $g_E =: (1 - \lambda^2)$ and $g_B =: 2\lambda^2$ with $\lambda \in [0, 1]$, as both strong and weak coupling regimes are recovered in the limits $\lambda \rightarrow 0$ and $\lambda \rightarrow 1$, respectively. This compactification is especially valuable for the following analysis, where the VQE minimization of the ground state for the SU(2) Yang-Mills toy model now samples the whole configuration space.

We simulate the described SSP ansatz from Section II B for the VQE first in an ideal setting without the coupling to the environment. The SSP variants of different depths are explicitly constructed in Section B, especially for the cut-off $j_{max} = 3/2$. In this section, we restrict to this cut-off, in which case the quantum number for each edge can be expressed with two qubits, i.e., $|q_{k,1}, q_{k,2}\rangle \equiv j_k \in \{0, 1/2, 1, 3/2\}$. Note that SSP requires up to two ancilla qubits (or more for even deeper variants than the ones used here), meaning that the total quantum resources for our toy model amount to 8 qubits (= 6 data + 1 or 2 ancillas). A more detailed overview of the key properties for each SSP and HEA is presented in table Table I in Section E. In our simulations, we employed the Powell optimization method due to its robustness to noise [58, 59], and adjusted the count of randomized starting candidates to increase linearly with the optimization-parameter count.

We start by comparing the performance of the newly introduced SSP with the conventional HEA. Note that both refer to families of ansätzen, e.g. we label SSP by the different counts $n = 2, 3, 4$ of gauge-invariant plaquette excitations to be added while preparing the ground state,

² Note that the Yang-Mills action [34] is defined by a single coupling constant. The second one emerges upon discretization when the Hamiltonian depends on the lattice spacing ϵ [35]. Recovery of the continuum requires the limit $\epsilon \rightarrow 0$ and a running of the coupling constants in form of a renormalization-group flow [57]. Here, we refrain from this extension and do not associate the coupling parameters with their continuum values.

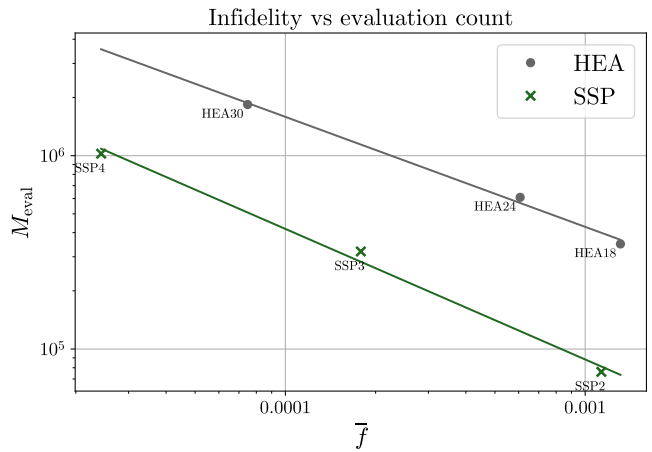


FIG. 3. Comparison of HEA (grey dots) and SSP (green crosses). Achieving a given infidelity \bar{f} (averaged over all λ) requires deeper circuits with more parameters and implies more function evaluations M_{eval} , i.e., calls to the quantum computer. For both ansätze, a fit (linear on the log-log scale) has been added as $M_{eval}(\bar{f}) = a \exp(b\bar{f})$ with fit parameters $(a, b) = (-0.5, 9)$ for HEA and $(a, b) = (-0.6, 6.7)$ for SSP respectively.

calling the respective variant SSP_n . Conversely, HEA_m denotes a variant with m many optimization parameters. With increasing optimization parameter count, equivalent to deeper circuits, the variants will sample larger portions of the Hilbert space. Consequently, it will always be possible to find within both families a variant that prepares a state $\psi(\theta_\lambda^*)$ approximating the ground state Ω better than a targeted infidelity

$$\bar{f} = \int_0^1 d\lambda f_\lambda, \quad f_\lambda = 1 - |\langle \Psi(\theta_\lambda^*) | \Omega_\lambda \rangle|^2, \quad (13)$$

averaged over all couplings λ . While low \bar{f} establishes suitable accuracy in applications, we must further ask how costly it is to reach it given an ansatz. Assuming fault-tolerant quantum computing, the limiting factor is the count of function evaluations, M_{eval} (i.e., the count of how often the expectation value has to be computed during the classical optimization procedure). Note that we define M_{eval} as the average number of function evaluations needed for the optimizer to converge to a local minimum given an arbitrary starting location. In fact, a mild scaling of M_{eval} is necessary for any VQE application to be feasible. In Figure 3, we compare the two families SSP and HEA to see how many evaluations M_{eval} are necessary to be better than a certain infidelity \bar{f} . Both (HEA18, HEA24, HEA30) and (SSP2, SSP3, SSP4) achieve lower infidelities \bar{f} with increasing number of optimization parameters, which requires more function evaluations (see Table I in Section E for details). As expected from the barren plateau problem, the dependence on evaluation count is exponentially related to the number of optimization parameters as can be seen

in the fitted exponential decay $M_{\text{eval}}(\bar{f})$ in Figure 3. To summarize: in the investigated regime, SSP outperforms HEA in terms of function evaluations.

As realistic quantum devices in the NISQ era are never noise-free, we take a closer look at the SSP3 variant and investigate its performance when coupled to the environment (see Section C and Section D for more details on the other circuits). In Figure 4, we present the best energy estimates for the ground state obtained from the VQE runs: In an idealized noise-free setting, for low λ values the short SSP3 circuit suffices, as the green triangles are close to the exact numerically determined solution $E_{0,j_{\text{max}}=3/2}$ shown in blue and computed in Section A. However, towards $\lambda \rightarrow 1$, the energies of the prepared ground states differ from the exact values, confirming that the true ground state requires more gauge-invariant excitations to approximate the analytically known solution at $\lambda = 1$, i.e., a Dirac- δ distribution centered at the unit elements of $SU(2)$.

Further, we simulate the LGT model by emulating the noise of contemporary quantum computers as explained in detail in Section C, built with a square lattice topology and such that each 2-qubit gate is assigned a 0.5% error. The presence of noise leads to an overall loss of accuracy, especially in the large λ limit. However, these noisy results, presented in red in Figure 4, should afterwards be processed with error mitigation tools. We outline in Section E the post-selection protocols applied, which can be used during the optimization procedure: projecting the prepared state back to the gauge-invariant Hilbert space and imposing rotational symmetry. At this stage, we are interested only in the best values from the minimization runs to determine the best-fit optimization parameters.³ While the VQE method targets the Hamiltonian at cut-off $j_{\text{max}} = 3/2$, shown in solid blue in Figure 4, the shaded area in light blue stems from the uncertainty due to the necessary cut-off error. Here, we computed the cut-off error exactly, yet future applications on larger systems need to replace this exact value by suitable approximations building upon [56].

C. Measurement of 2-point correlators

Given the optimal parameter set $\bar{\theta}^*$, the SSP method creates the target state $\psi(\bar{\theta}^*)$ close to the exact ground state Ω of the toy model. Using this state, we prepare the vacuum to study physical properties of the model. Primarily, we aim to analyze the different phases of the LGT model. To distinguish these from each other, we need to

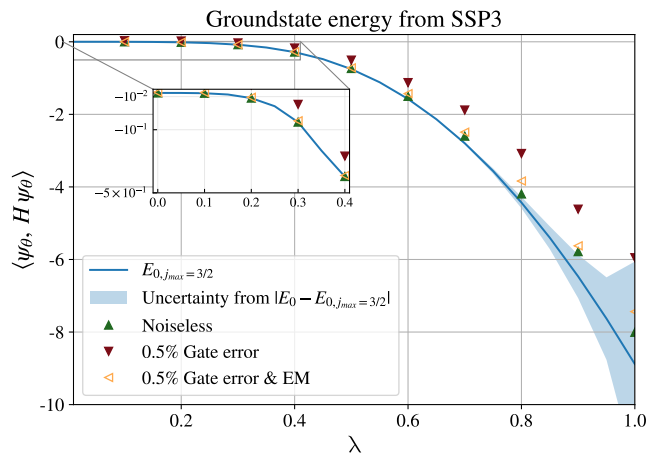


FIG. 4. Best achieved minima for the energy expectation values for SSP3, a particular variant of the SSP circuit which creates $n = 3$ gauge-invariant plaquette excitations. The VQE has been emulated in an ideal environment (green) and in the presence of noise from a 0.5% 2-qubit gate error (red). Upon adding error mitigation (EM) protocols (orange), the accuracy comes close to the exact energies (blue) and falls within the uncertainty given by the finite cut-off $j_{\text{max}} = 3/2$ (shaded region).

introduce a suitable gauge-invariant observable. We outline in Section A how the toy model of the 6-valent vertex naturally gives rise to a gauge-invariant, discretized version of the 2-point correlator, symbolically written to as $\langle \Omega | (A_a^I A_b^J)^G | \Omega \rangle$. Once the ground state Ω of the theory has been prepared for a given coupling parameter λ , we use it to measure the expectation value of said 2-point correlator. Analyzing these correlations allows one to identify the coupling-dependent phases of the model. Based on symmetry arguments, the non-vanishing terms of the 2-point correlator of the toy model must be of the form (see Section A for details)

$$\langle \Omega | (A_a^I A_b^J)^G | \Omega \rangle = \delta_{IJ} c_P(\lambda) \quad (14)$$

where $a \neq b$ and $c_P(\lambda)$ is obtained by evaluating the expectation value of a Pauli decomposition of that operator. The 2-point correlator is shown in Figure 5. Here, the best optimized $\bar{\theta}^*$ from the simulations shown in Figure 4 have been used to prepare the ground state with a sample size of 1,000 and the median shown as orange data points cleaned in post-processing analysis as outlined before. The error bars denote the standard deviation centered around the mean of the histogram population. After error mitigation, the different phases for the coupling parameter can be clearly distinguished⁴: the

³ Conceptually, re-running a state preparation algorithm with the same setting gives spread-out results due to the presence of noise, which affects the found optimum in a single run – but these effects are not taken into account in Figure 4, which presents a single optimization run.

⁴ Note that in the presence of a cut-off j_{max} , the system is finite-dimensional, thus not exhibiting true “phase transitions”. We refer to *facsimile* phases in the following, whose properties are expected to hold when taking the corresponding limit $j_{\text{max}} \rightarrow \infty$.

uncorrelated phase defined by $c_p \approx 0$ dominates the limit $\lambda \rightarrow 0$, and correlations between the different directions of the lattice emerge for large $\lambda \rightarrow 1$ values, indicated by $c_p \approx \mathcal{O}(1)$. The system slowly undergoes a gradual crossover (phase transition) for intermediate λ . In fact, independent of the depth of SSP used for ground state preparation, the crossover is observed in the same region. At the simulated 0.5% gate-error level, the exact correlator values cannot be reached for all $\lambda \in [0, 1]$.

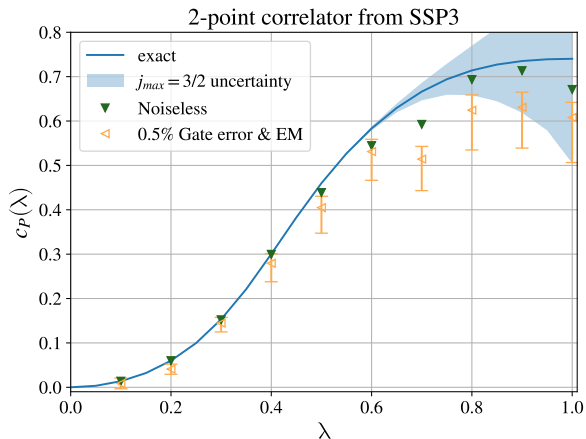


FIG. 5. 2-point correlator evaluated on $\psi(\vec{\theta}^*)$ prepared with the best optimization parameters found in Figure 11. Green triangles show ideal values, and orange points show error-mitigated and post-selected results. Data points indicate median and error bars indicate standard deviation centered around the mean. In blue is the exact correlator shown with a shaded uncertainty region due to the finite cut-off $j_{max} = 3/2$.

IV. DISCUSSION

We introduced the SSP protocol to investigate ground state preparation via VQE on quantum hardware for non-Abelian LGTs. Although the scalability of VQE in general remains an open question, we alleviate some of its challenges, e.g. the barren plateau problem, by using the SSP ansatz. Its potential for scaling to larger lattice sizes rests on projecting onto the spin-network basis, thereby reducing the required qubit resources for representing the system. Additionally, by preserving gauge invariance during creation of the ground state, it reduces the optimization parameter count. The reduction of required optimization parameters makes the SSP ansatz particularly attractive for the late NISQ era, where qubit numbers and gate fidelities have matured to a level at which VQE is limited by the barren plateau problem.

We demonstrated the feasibility of SSP in a classically symmetry-restricted $d = 3$ pure $SU(2)$ Yang-Mills toy model consisting of a single 6-valent vertex. In an ideal

setting, SSP achieves arbitrary accuracy by successively increasing circuit depth. Even in the presence of the noise expected from contemporary quantum hardware, the usual error-mitigation schemes can help to restore accuracy. A comparison between SSP and HEA unveiled that SSP needs consistently fewer function evaluations to converge, thereby alleviating the barren plateau problem. As this is tied to the smaller count of optimization parameters for SSP compared to HEA, we expect this to hold also when scaling to larger lattice sizes, where the fraction of physical states tilts further in favor of SSP. Finally, the prepared ground state was used to extract physical properties, such as the 2-point correlator, which qualitatively detects phase transitions directly from measurements on the quantum device.

To go further and use the SSP ansatz in regimes beyond classical simulatability, more work is required: to avoid an unfavorable scaling in the number of optimization candidates, one should add an adiabatic ramp-up protocol for large lattices. Additionally, the iterative nature of inserting more excitations into the system until convergence is reached is beneficial in conjunction with the scalable ADAPT-VQE framework, which dynamically adapts the algorithm during the optimization procedure [60]. Finally, moving from the ancilla-based approach to using the plaquette excitations as basic excitations in a unitary coupled cluster ansatz [61] can make the algorithm more dense. In summary, a straightforward path to extending SSP is apparent.

Once such states are prepared, one can place initial matter configurations on it to study dynamical evolution [12] or obtain insights into the mass gap, e.g., by scaling the system to larger sizes and investigating its asymptotic behavior. We reserve these topics for future research.

ACKNOWLEDGEMENTS

We thank Jad Halimeh, Giovanni Cataldi, Emanuele Mendicelli, Saeed Rastgoo, Jorden Roberts, Federica Fragomeno, Philipp Aumann, and Arya Suneesh for insightful discussions and helpful comments at various stages of this article. We are grateful for many discussions with the QC4HEP consortium. This work received financial support from the German Federal Ministry of Education and Research via the funding program under contract number 13N16188 (MUNIQ-SC) and under contract number 13N15680 (GeQCoS), as well as by the European Union by the EU Flagship on Quantum Technology HORIZON-CL4-2022-QUANTUM-01-SGA project 101113946 OpenSuperQ-Plus100 and MOlecular Quantum Simulations (MOQS) (Grant-Nr. 955479). The research is part of the Munich Quantum Valley, which is supported by the Bavarian state government with funds from the Hightech Agenda Bayern Plus initiative.

-
- [1] A. Jaffe and E. Witten, [Yang–mills existence and mass gap](#), Millennium Prize Problems, Clay Mathematics Institute (2000), accessed: 2025-08-30.
- [2] T. Balaban, Propagators and renormalization transformations for lattice gauge theories. i, *Communications in Mathematical Physics* **95**, 17 (1984).
- [3] D. J. Wilson, R. A. Briceño, J. J. Dudek, R. G. Edwards, and C. E. Thomas (for the Hadron Spectrum Collaboration), Quark-mass dependence of elastic πk scattering from qcd, *Phys. Rev. Lett.* **123**, 042002 (2019).
- [4] P. Fontana and A. Trombettoni, Mean field approaches to lattice gauge theories: A review, *Entropy* **27**, 250 (2025).
- [5] R. Brower, N. Christ, C. DeTar, R. Edwards, and P. Mackenzie, Lattice qcd application development within the us doe exascale computing project, *EPJ Web of Conferences* **175**, 09010 (2018).
- [6] E. Rico, T. Pichler, M. Dalmonte, P. Zoller, and S. Montangero, Tensor networks for lattice gauge theories and atomic quantum simulation, *Phys. Rev. Lett.* **112**, 201601 (2014).
- [7] P. Silvi, E. Rico, T. Calarco, and S. Montangero, Lattice gauge tensor networks, *New Journal of Physics* **16**, 103015 (2014).
- [8] F. Verstraete, V. Murg, and J. I. Cirac, Matrix product states, projected entangled pair states, and variational renormalization group methods for quantum spin systems, *Advances in Physics* **57**, 143 (2008).
- [9] C. A. W. et al., Quantum computing for high-energy physics: State of the art and challenges, *PRX Quantum* **5**, 037001 (2024).
- [10] B. Y. et al., Observation of gauge invariance in a 71-site bose–hubbard quantum simulator, *Nature* **587**, 392–396 (2020).
- [11] M. C. Bañuls and K. Cichy, Review on novel methods for lattice gauge theories, *Reports on Progress in Physics* **83**, 024401 (2020).
- [12] T. A. Cochrane, B. Jobst, E. Rosenberg, Y. D. Lensky, G. Gyawali, N. Eassa, M. Will, D. Abanin, R. Acharya, L. Aghababaie Beni, T. I. Andersen, M. Ansmann, F. Arute, K. Arya, A. Asfaw, J. Atalaya, R. Babbush, B. Ballard, and ..., Visualizing dynamics of charges and strings in (2+1)d lattice gauge theories, *Nature* **642**, 315 (2025).
- [13] J. Mildenberger, W. Mruczkiewicz, J. C. Halimeh, Z. Jiang, and P. Hauke, Probing confinement in a \mathbb{Z}_2 lattice gauge theory on a quantum computer, *arXiv preprint* (2022), [arXiv:2203.08905 \[quant-ph\]](#).
- [14] C. Schweizer, F. Grusdt, M. Berngruber, L. Barbiero, E. Demler, N. Goldman, I. Bloch, and M. Aidelsburger, Floquet approach to \mathbb{Z}_2 lattice gauge theories with ultracold atoms in optical lattices, *Nature Physics* **15**, 1168 (2019).
- [15] E. A. Martinez, C. A. Muschik, P. Schindler, D. Nigg, A. Erhard, M. Heyl, P. Hauke, M. Dalmonte, T. Monz, P. Zoller, and R. Blatt, Real-time dynamics of lattice gauge theories with a few-qubit quantum computer, *Nature* **534**, 516 (2016).
- [16] D. Banerjee, M. Dalmonte, M. Müller, E. Rico, P. Stebler, U.-J. Wiese, and P. Zoller, Atomic quantum simulation of dynamical gauge fields coupled to fermionic matter, *Physical Review Letters* **109**, 175302 (2012).
- [17] D. Marcos, P. Rabl, E. Rico, and P. Zoller, Superconducting circuits for quantum simulation of dynamical gauge fields, *Physical Review Letters* **111**, 110504 (2013).
- [18] S. Dusuel and J. Vidal, Mean-field ansatz for topological phases with string tension, *Physical Review B* **92**, 125150 (2015).
- [19] K. Lee, F. Turro, and X. Yao, Quantum computing for energy correlators, *Physical Review Letters* **131**, 171902 (2023).
- [20] N. Klco, M. J. Savage, and J. R. Stryker, Su(2) non-abelian gauge field theory in one dimension on digital quantum computers, *Physical Review D* **101**, 074512 (2020), [arXiv:1908.06935 \[quant-ph\]](#).
- [21] G. Calajó, G. Magnifico, C. Edmunds, M. Ringbauer, S. Montangero, and P. Silvi, Digital quantum simulation of a (1+1)d su(2) lattice gauge theory with ion qudits, *PRX Quantum* **5**, 040309 (2024).
- [22] A. Mezzacapo, E. Rico, C. Sabín, I. L. Egusquiza, L. Lamata, and E. Solano, Non-abelian su(2) lattice gauge theories in superconducting circuits, *Phys. Rev. Lett.* **115**, 240502 (2015).
- [23] E. Mendicelli, Investigating how to simulate gauge theories on a quantum computer, *arXiv* (2023), [2308.15421 \[hep-lat\]](#).
- [24] T. V. Zache, D. Gonzalez-Cuadra, and P. Zoller, Quantum and classical spin-network algorithms for q-deformed kogut-susskind gauge theories, *Physical Review Letters* **131**, 171902 (2023).
- [25] J. R. McClean, J. Romero, R. Babbush, and A. Aspuru-Guzik, The theory of variational hybrid quantum-classical algorithms, *New Journal of Physics* **18**, 023023 (2016).
- [26] A. Peruzzo, J. McClean, P. Shadbolt, M.-H. Yung, X.-Q. Zhou, P. J. Love, A. Aspuru-Guzik, and J. L. O’Brien, A variational eigenvalue solver on a photonic quantum processor, *Nature Communications* **5**, 4213 (2014).
- [27] A. Kandala, A. Mezzacapo, K. Temme, M. Takita, M. Brink, J. M. Chow, and J. M. Gambetta, Hardware-efficient variational quantum eigensolver for small molecules and quantum magnets, *Nature* **549**, 242 (2017).
- [28] K. Bharti, A. Cervera-Lierta, T. H. Kyaw, T. Haug, S. Alperin-Lea, A. Anand, M. Degroote, H. Heimonen, J. S. Kottmann, T. Menke, W.-K. Mok, S. Sim, L.-C. Kwek, and A. Aspuru-Guzik, Noisy intermediate-scale quantum algorithms, *Reviews of Modern Physics* **94**, 015004 (2022).
- [29] K. Temme, S. Bravyi, and J. M. Gambetta, Error mitigation for short-depth quantum circuits, *Physical Review Letters* **119**, 180509 (2017).
- [30] K. Liegener, O. Morsch, and G. Pupillo, Solving quantum chemistry problems on quantum computers, *Physics Today* **77**, 34 (2024).
- [31] R. Penrose, Angular momentum: An approach to combinatorial space-time, in *Quantum Theory and Beyond*, edited by T. Bastin (Cambridge University Press, 1971) pp. 151–180.
- [32] C. Rovelli and L. Smolin, Spin networks and quantum gravity, *Physical Review D* **52**, 5743 (1995).
- [33] J. C. Baez, Spin network states in gauge theory, *Advances in Mathematics* **117**, 253 (1996).

- [34] C. N. Yang and R. L. Mills, Conservation of isotopic spin and isotopic gauge invariance, *Phys. Rev.* **96**, 191 (1954).
- [35] J. Kogut and L. Susskind, Hamiltonian formulation of wilson's lattice gauge theories, *Phys. Rev. D* **11**, 395 (1975).
- [36] V. Guillemin and S. Sternberg, *Semi-classical Analysis* (International Press, 2013).
- [37] T. Balaban, Renormalization group approach to lattice gauge theories. i. generation of effective actions in a small field approximation and a coupling constant renormalization in four dimensions, *Communications in Mathematical Physics* **89**, 571 (1983).
- [38] A. Ashtekar and J. Lewandowski, Projective techniques and functional integration for gauge theories, *Journal of Mathematical Physics* **36**, 2170 (1995).
- [39] T. Thiemann, *Modern canonical quantum general relativity*, Cambridge University Press (2007).
- [40] I. D'Andrea, C. W. Bauer, D. M. Grabowska, and M. Freytsis, New basis for hamiltonian su(2) simulations, *Phys. Rev. D* **109**, 074501 (2024).
- [41] G. Cataldi, G. Magnifico, P. Silvi, and S. Montangero, Simulating (2+1)D su(2) yang-mills lattice gauge theory at finite density with tensor networks, *Phys. Rev. Res.* **6**, 033057 (2024).
- [42] F. Peter and H. Weyl, Die vollständigkeit der primitiven darstellungen einer geschlossenen kontinuierlichen gruppe, *Mathematische Annalen* **97**, 737 (1927).
- [43] E. P. Wigner, *Group theory and its application to the quantum mechanics of atomic spectra*, Academic Press (1959).
- [44] D. M. Brink and G. R. Satchler, *Angular Momentum*, 3rd ed. (Oxford University Press, 1993).
- [45] S. V. Mathis, G. Mazzola, and I. Tavernelli, Toward scalable simulations of lattice gauge theories on quantum computers, *Physical Review D* **102**, 10.1103/physrevd.102.094501 (2020).
- [46] J. R. McClean, S. Boixo, V. N. Smelyanskiy, R. Babbush, and H. Neven, Barren plateaus in quantum neural network training landscapes, *Nature Communications* **9**, 4812 (2018).
- [47] S. Wang, E. Fontana, M. Cerezo, K. Sharma, A. Sone, L. Cincio, and P. J. Coles, Noise-induced barren plateaus in variational quantum algorithms, *Nature Communications* **12**, 6961 (2021).
- [48] M. Cerezo, A. Sone, T. Volkoff, L. Cincio, and P. J. Coles, Cost function dependent barren plateaus in shallow parametrized quantum circuits, *Nature Communications* **12**, 1791 (2021).
- [49] D. Wecker, M. B. Hastings, and M. Troyer, Progress towards practical quantum variational algorithms, *Physical Review A* **92**, 10.1103/physreva.92.042303 (2015).
- [50] L. Zhu, S. Liang, C. Yang, and X. Li, *Optimizing shot assignment in variational quantum eigensolver measurement* (2024), arXiv:2307.06504 [quant-ph].
- [51] D. Marolf, Group averaging and refined algebraic quantization: Where are we now?, arXiv preprint gr-qc/0011112 (2000), arXiv:gr-qc/0011112.
- [52] G. Magnifico, G. Cataldi, M. Rigobello, P. Majcen, D. Jaschke, P. Silvi, and S. Montangero, Tensor networks for lattice gauge theories beyond one dimension: a roadmap, arXiv preprint arXiv:2407.03058 (2024), arXiv:2407.03058 [hep-lat].
- [53] G. Cataldi, G. Magnifico, P. Silvi, and S. Montangero, (2+1)d su(2) yang-mills lattice gauge theory at finite density with tensor networks, arXiv preprint arXiv:2307.09396 (2023), arXiv:2307.09396 [hep-lat].
- [54] Z. Holmes, K. Sharma, M. Cerezo, and P. J. Coles, Connecting ansatz expressibility to gradient magnitudes and barren plateaus, *PRX Quantum* **3**, 010313 (2022).
- [55] W. Kamiński and K. Liegener, Symmetry restriction and its application to gravity, arXiv preprint arXiv:2009.06311 10.1088/1361-6382/abdf29 (2020), submitted on 14 September 2020; 69 pages, arXiv:2009.06311 [gr-qc].
- [56] A. N. Ciavarella, S. Hariprakash, J. C. Halimeh, and C. W. Bauer, Truncation uncertainties for accurate quantum simulations of lattice gauge theories, arXiv preprint arXiv:2508.00061 (2025), submitted 31 Jul 2025; 27 pages, 8 figures.
- [57] T. Lang, K. Liegener, and T. Thiemann, Hamiltonian renormalisation i: Derivation from osterwalder-schrader reconstruction, arXiv preprint arXiv:1711.05685 (2017), arXiv:1711.05685 [math-ph].
- [58] M. J. D. Powell, An efficient method for finding the minimum of a function of several variables without calculating derivatives, *The Computer Journal* **7**, 155 (1964).
- [59] P. Virtanen, R. Gommers, T. E. Oliphant, M. Haberland, T. Reddy, D. Cournapeau, E. Burovski, P. Peterson, W. Weckesser, J. Bright, S. J. van der Walt, M. Brett, J. Wilson, K. J. Millman, N. Mayorov, A. R. J. Nelson, E. Jones, R. Kern, E. Larson, C. J. Carey, Í. Polat, Y. Feng, E. W. Moore, J. VanderPlas, D. Laxalde, J. Perktold, R. Cimrman, I. Henriksen, E. A. Quintero, C. R. Harris, A. M. Archibald, A. H. Ribeiro, F. Pedregosa, P. van Mulbregt, and S. . Contributors, Scipy 1.0: Fundamental algorithms for scientific computing in python, *Nature Methods* **17**, 261 (2020).
- [60] H. R. Grimsley, S. E. Economou, E. Barnes, and N. J. Mayhall, An adaptive variational algorithm for exact molecular simulations on a quantum computer, *Nature Communications* **10**, 3007 (2019).
- [61] P. J. J. O'Malley, R. Babbush, I. D. Kivlichan, J. Romero, J. R. McClean, R. Barends, J. Kelly, P. Roushan, A. Tranter, N. Ding, E. Campbell, Y. Chen, Z. Chen, B. Chiaro, A. Dunsworth, E. Jeffrey, A. Megrant, J. Mutus, M. Neeley, C. Neill, C. Quintana, D. Sank, A. Vainsencher, J. Wenner, T. White, P. J. Love, A. Aspuru-Guzik, A. N. Cleland, and J. M. Martinis, Scalable quantum simulation of molecular energies, *Physical Review X* **6**, 031007 (2016).
- [62] E. P. Wigner, On the matrices which reduce the kronecker products of representations of simply reducible groups, *Proceedings of the National Academy of Sciences of the USA* **26**, 106 (1940).
- [63] G. Racah, Theory of complex spectra. ii, *Physical Review* **62**, 438 (1942).
- [64] D. Mattern, Simulating the 1-vertex model of su(2) lattice gauge theory on near term quantum computers, Bachelor thesis, TUM (2024).
- [65] A. Barenco, C. H. Bennett, R. Cleve, D. P. DiVincenzo, N. Margolus, P. Shor, T. Sleator, J. A. Smolin, and H. Weinfurter, *Elementary gates for quantum computation* (1995).
- [66] A. Watkins, M. Sivak, J. Moreira, L. Capelluto, A. W. Cross, J. M. Gambetta, D. C. McKay, T. Alexander, and et al., Qiskit: An open-source framework for quantum computing, *Nature Reviews Physics* **5**, 349 (2023).

- [67] T. Alexander, L. Capelluto, J. Gacon, C. Granade, D. Greenberg, W. Guan, A. Javadi-Abhari, N. Kanazawa, A. Kononov, D. Liu, M. Marques, D. C. McKay, J. Moreira, M. Motta, P. D. Nation, A. Paz, M. Pistoia, E. Pritchett, W. Ray, M. Reed, A. Schwab-Molzen, I. Sertage, M. Singh, S. Sivarajah, M. Takita, C. J. Wood, J. R. Wootton, T. Yu, and J. M. Gambetta, Qiskit aer: A high performance simulator framework for quantum circuits, [arXiv preprint arXiv:2008.08571](#) (2020), [arXiv:2008.08571 \[quant-ph\]](#).
- [68] G. Huber, F. Roy, L. Koch, I. Tsitsilin, J. Schirk, N. Glaser, N. Bruckmoser, C. Schweizer, J. Romeiro, G. Krylov, M. Singh, F. Haslbeck, M. Knudsen, A. Marx, F. Pfeiffer, C. Schneider, F. Wallner, D. Bunch, L. Richard, L. Södergren, K. Liegener, M. Werninghaus, and S. Filipp, Parametric multi-element coupling architecture for coherent and dissipative control of superconducting qubits, [arXiv preprint arXiv:2403.02203](#) (2024), [quant-ph].
- [69] M. Ivezic, [The race toward ftqc: Ocelot, majorana, willow, heron, zuchongzhi](#) (2025), accessed: 2025-09-01.
- [70] G. Q. AI, [Willow spec sheet](#) (2024), accessed: 2025-09-01.
- [71] S. Sim, P. D. Johnson, and A. Aspuru-Guzik, Expressibility and entangling capability of parameterized quantum circuits for hybrid quantum-classical algorithms, [Advanced Quantum Technologies](#) **2**, 1900070 (2019).
- [72] S. McArdle, S. Endo, A. Aspuru-Guzik, S. C. Benjamin, and X. Yuan, Quantum computational chemistry, [Rev. Mod. Phys.](#) **92**, 015003 (2020), [arXiv:1808.10402 \[quant-ph\]](#).
- [73] X. Bonet-Monroig, R. Sagastizabal, M. Singh, and T. E. O'Brien, Low-cost error mitigation by symmetry verification, [Physical Review A](#) **98**, 062339 (2018), [arXiv:1807.10050 \[quant-ph\]](#).
- [74] S. McArdle, X. Yuan, and S. Benjamin, Error-mitigated digital quantum simulation, [Physical Review Letters](#) **122**, 180501 (2019), [arXiv:1807.02467 \[quant-ph\]](#).
- [75] B. Edoardo, M. Julius, M. W. Matteo, and H. Philipp, Symmetry verification for noisy quantum simulations of non-abelian lattice gauge theories, [arXiv abs/2412.07844](#) (2025), accepted in *Quantum* 2025-06-26; published under CC-BY 4.0, [arXiv:2412.07844 \[quant-ph\]](#).

Appendix A: Computations on the gauge-invariant Hilbert space

This appendix outlines the details behind the toy model motivated in Section III A when described in terms of spin-network functions. The gauge theory is defined by holonomies $h \in \text{SU}(2)$ and gauge covariant fluxes $P \in \mathfrak{su}(2)$ subject to the *holonomy-flux algebra*:

$$[h(e), P_I(e')] = h(e)\tau_I\delta_{ee'} \quad (\text{A1})$$

$$[P_I(e), P_J(e')] = \epsilon_{IJK}P_K(e)\delta_{ee'} \quad (\text{A2})$$

and all other commutators vanish identically. The ϵ_{IJK} are the structure functions of the corresponding Lie algebra and τ_I a suitable basis, i.e., $\tau_I \in \mathfrak{su}(2)$ for the Lie

group $\text{SU}(2)$ used throughout this manuscript.⁵ We recall from the main text that the kinematical Hilbert space at any 6-valent vertex in a $d = 3$ lattice can be expressed in terms of ingoing edges $e_k^- \in \gamma$ and outgoing edges $e_k^+ \in \gamma$ with $k = 1, 2, 3$. Using the Peter&Weyl theorem [42] for each edge, the full tensor product Hilbert space takes the form $\mathcal{H} = \otimes_e \mathcal{H}_e$ with basis elements

$$\prod_{k=1,2,3} D_{m_k^+ n_k^+}^{j_k^+}(h_k^+) D_{m_k^- n_k^-}^{j_k^-}(h_k^-). \quad (\text{A3})$$

The toy model under consideration is based on periodic boundary conditions, which we enforce by restricting to the following case (including a suitable relabeling)

$$j_k^+ = j_k^- = j_k, \quad n_k^+ = m_k^- = \nu_k, \quad (\text{A4})$$

$$m_k^+ = m_k, \quad n_k^- = n_k \quad (\text{A5})$$

and a summation over the twice appearing index ν_k . Under this restriction, the system simplifies as its wave function will depend only on the three combinations of the form $h_k^+ h_k^- \in \text{SU}(2)$, i.e., three independent copies over $\text{SU}(2)$. Further, the restriction to the gauge-invariant Hilbert space \mathcal{H}_G can now be performed in the usual manner by contracting with a six-valent intertwiner. For the computation in this paper, we pick a specific basis of intertwiners on the cubic lattice labeled by the auxiliary irreps $\pi_k^v, k = 1, 2, 3$ over the unit in $\text{SU}(2)$. Those and the irreps j_k^\pm are contracted in suitable triples with Wigner-3j-symbols [43], i.e., the 3-valent intertwiners:

$$\begin{aligned} \iota_{m_1 m_2 m_3, n_1, n_2, n_3}^{v, \pi_+, \pi_o, \pi_-} &:= \sum_{\rho_+, \rho_o, \rho_-} \begin{pmatrix} j_1^+ & j_2^+ & \pi_+ \\ m_1 & m_2 & \rho_+ \end{pmatrix} \times \quad (\text{A6}) \\ &\times \begin{pmatrix} \pi_+ & j_3^+ & \pi_o \\ \rho_+ & m_3 & \rho_o \end{pmatrix} \begin{pmatrix} \pi_o & j_3^- & \pi_- \\ \rho_o & n_3 & \rho_- \end{pmatrix} \begin{pmatrix} j_1^- & j_2^- & \pi_- \\ n_1 & n_2 & \rho_- \end{pmatrix}, \end{aligned}$$

where j_k^+ stands for the irrep of the outgoing edge at v and j_k^- for the irrep of the ingoing edge in direction k , respectively. By this, we obtain the full spin-network functions describing the kinematical Hilbert space of the theory, characterized by a total of six quantum numbers:

$$T_{j_1, j_2, j_3, \pi_+, \pi_o, \pi_-}(\vec{h}) =: \langle \vec{h} | j_1, j_2, j_3; \pi_+, \pi_o, \pi_- \rangle. \quad (\text{A7})$$

To study a $\text{SU}(2)$ Yang-Mills theory in this setting, we need to define a suitable discretization of the Hamiltonian on this lattice, which we construct with maximal similarity to the Kogut-Susskind Hamiltonian [35]:

$$H = g_E \sum_e H_E(e) - g_B \sum_{\square} H_B(\square), \quad (\text{A8})$$

$$H_E(e) = \delta^{IJ} P_I(e) P_J(e), \quad (\text{A9})$$

$$H_B(\square) = \text{tr}(h(\square) + h(\square)^\dagger). \quad (\text{A10})$$

The fact that the minimal plaquettes are spanned by only two quantum numbers (instead of four on larger lattices)

⁵ A common choice is $\tau_I = -i\sigma_I/2$ with σ_I being the Pauli matrices.

motivates recalling the regularization procedure of the continuum expression, explicitly of the curvature of the connection $F(A) := dA + A \wedge A$. Following the non-Abelian Stokes theorem, which states that

$$F_{ab}^I e^a e^b F_{cd}^J e^c e^d \delta_{IJ} \approx (1 - \text{tr}(\text{Re}(h(\square_{ab}))))/\epsilon^4 \quad (\text{A11})$$

for any closed plaquette \square of size ϵ^2 which starts at v and has tangents oriented along the coordinate directions a, b spanned by the normal vectors $(e^a)_k = \delta_k^a$. Note that there is no requirement to choose whether the tangents point in positive or negative direction, and we are free to choose a manifestly positive orientation at v , i.e., choose our plaquette to be oriented leaving along j_a^+ and returning along j_b^+ . Approximating $F_{ab} F^{ab}$ in such a way leads to the following regularization of the Hamiltonian for the single 6-valent vertex graph:

$$H = (1 - \lambda^2) \sum_a P^I(e_a^+) P_I(e_a^+) - 2\lambda^2 \sum_{ab} \text{tr}(\text{Re}(h(e_a^+) h(e_b^+)^\dagger)). \quad (\text{A12})$$

Note that for the coupling constants we used, a total rescaling of the Hamiltonian does not change the qualitative physics but only leads to a rescaling, essentially reducing us to a single parameter that specifies the relative weight between H_E and H_B . Further, we compactified the interval of said weight $[0, \infty]$ to the finite region $\lambda \in [0, 1]$. Computing the matrix elements of (A12) in the basis of (A11) can now be done using the usual angular momentum recoupling theory, see [44] for extensive guides. The basic equations used here are the recoupling of Wigner D-functions

$$D_{m_1 n_1}^{(j_1)}(h) D_{m_2 n_2}^{(j_2)}(h) = \sum_{j_3=|j_1-j_2|}^{j_1+j_2} \sum_{m_3, n_3} d_{j_3} (-1)^{n_3-m_3} \times \begin{pmatrix} j_1 & j_2 & j_3 \\ m_1 & m_2 & m_3 \end{pmatrix} \begin{pmatrix} j_1 & j_2 & j_3 \\ n_1 & n_2 & n_3 \end{pmatrix} D_{-m_3, -n_3}^{(j_3)}(h), \quad (\text{A13})$$

the orthogonality relations between 3j-symbols

$$\sum_{j_3, m_3} d_{j_3} \begin{pmatrix} j_1 & j_2 & j_3 \\ m_1 & m_2 & m_3 \end{pmatrix} \begin{pmatrix} j_1 & j_2 & j_3 \\ m'_1 & m'_2 & m_3 \end{pmatrix} = \delta_{m_1, m'_1} \delta_{m_2, m'_2} \quad (\text{A14})$$

$$\sum_{m_1, m_2} d_{j_3} \begin{pmatrix} j_1 & j_2 & j_3 \\ m_1 & m_2 & m_3 \end{pmatrix} \begin{pmatrix} j_1 & j_2 & j'_3 \\ m_1 & m_2 & m'_3 \end{pmatrix} = \delta_{j_3, j'_3} \delta_{m_3, m'_3} \quad (\text{A15})$$

and the definition of the 6j-symbol [62, 63]:

$$\left\{ \begin{matrix} a & b & c \\ d & e & f \end{matrix} \right\} = \sum_{\substack{\alpha, \beta, \gamma, \delta \\ \epsilon, \phi}} (-1)^{(d+e+f+\delta+\epsilon+\phi)} \begin{pmatrix} a & b & c \\ \alpha & \beta & \phi \end{pmatrix} \times \begin{pmatrix} a & e & f \\ \alpha & \epsilon & -\phi \end{pmatrix} \begin{pmatrix} d & b & f \\ -\delta & \beta & \phi \end{pmatrix} \begin{pmatrix} d & e & c \\ \delta & -\epsilon & \gamma \end{pmatrix}. \quad (\text{A16})$$

Upon performing this computation of matrix elements of the Hamiltonian explicitly, it becomes apparent that [64]

$$\langle \vec{j}', \pi'_+, \pi'_o, \pi'_- | H[\vec{j}, \pi_+, \pi_o, \pi_-] \rangle \propto \delta_{\pi'_o, \pi_o}. \quad (\text{A17})$$

In other words, the Hamiltonian decomposes into superselection sectors, as the label π_o never gets changed during the action of the Hamiltonian and is thus a conserved quantity. It follows that the eigenstates of the Hamiltonian must be supported in each superselection sector separately. In this article, we focus therefore on the superselection sector $\pi_o = 0$ as the ground state is found in this sector for $\lambda = 0$, in which case the solution is analytically known to be $j_k = 0$, hence enforcing $\pi_k = 0$ as well. Being interested in how this state changes with $\lambda \rightarrow 1$ requires numerical analysis.

Focusing in what follows on $\pi_o = 0$ will, due to the 3j-symbols in $l^{v_o, \pi_+, \pi_o, \pi_-}$, enforce that $\pi_\pm = j_\pm^s = j_3$. This reduces the full physical Hilbert space of the superselection sector $\pi_o = 0$ to one characterized by three quantum numbers j_1, j_2, j_3 , and hence makes it isomorphic to the Hilbert space over three edges that are contracted with two distinct 3j-symbols, graphically envisioned as a Θ -graph. The spin-network functions forming the basis of this space are hence labeled as

$$T_{\vec{j}}(\vec{h}) = \langle \vec{h} | j_1, j_2, j_3 \rangle = \langle \vec{h} | \vec{j} \rangle. \quad (\text{A18})$$

Using (A13)-(A16), we compute the matrix elements in this basis, i.e., the electric part:

$$\langle j'_1, j'_2, j'_3 | H_E(e_a) | j_1, j_2, j_3 \rangle = j_a (j_a + 1) \delta_{j_1, j'_1} \delta_{j_2, j'_2} \delta_{j_3, j'_3} \quad (\text{A19})$$

and the magnetic part, here for the plaquette $a = 1, b = 2$: [64]

$$\langle j'_1, j'_2, j'_3 | H_{\square_{12}} | j_1, j_2, j_3 \rangle = \sqrt{d_{j_1} d_{j'_1} d_{j_2} d_{j'_2}} \times \begin{Bmatrix} j_1 & j_2 & j_3 \\ j'_2 & j'_1 & 1/2 \end{Bmatrix}^2 \delta_{j_1, j'_1 \pm 1/2} \delta_{j_2, j'_2 \pm 1/2} \delta_{j_3, j'_3}. \quad (\text{A20})$$

We note that, in general, any gauge-invariant observable can be written in such an explicit form, making the spin-network basis a suitable tool for numerical investigations. A physically interesting example would be the 2-point correlator: This is a relevant observable in high-energy physics to track the correlation between different spatial regions of the system, symbolically referred to as the vacuum expectation value of the field operators $\langle \Omega | A_a(x) A_b(y) | \Omega \rangle$. However, in LGT, one needs to introduce a suitable regularization of $A_a(x)$ on the lattice and then, moreover, ensure that the complete observable is gauge-invariant. For both steps, there is a custom procedure in the literature: first, $A_a(v_o) \approx (h(e_a) - 1)/\epsilon$ and any observable \mathcal{O}_γ on the lattice γ might be projected onto its gauge invariant version via the procedure of group averaging:

$$\mathcal{O}_\gamma^G(\vec{h}) := \left(\prod_{v \in \gamma} \int_{SU(2)} d\mu_H(g_v) \right) \mathcal{O}_\gamma(\{g_{e(0)} h_e g_{e(1)}^\dagger\}_{e \in \gamma}). \quad (\text{A21})$$

However, on large lattices, concatenating both procedures for the 2-point correlator $\langle \Omega, A_a(x) A_b(y) \Omega \rangle$ actually annihilates the expression when x and y are spatially separated, because of the open endpoints of their

edges. Yet, for the single-vertex graph, it is necessary that $x = y = v_o$, and even if $a \neq b$, the starting and end points of the edges in both directions agree. This renders a non-trivial expression and *allows to define a finite 2-point correlator on the single vertex graph*. Explicitly one obtains: [64]

$$(A_a^I(v_o)A_b^J(v_o))^G = \frac{1}{3}\delta_{IJ}(\text{tr}(h(e_a)h(e_b)^\dagger) - \text{tr}(h(e_a)h(e_b))) \quad (\text{A22})$$

To compute the matrix elements of this operator on the 6-valent vertex, note that $h(e_b)^\dagger$ means traversing the edge e_b in the opposite direction of $h(e_b)$. Hence, no matter the orientation chosen, one of the two terms in (A22) will require a two-edge one leaving in direction j^+ , the other in direction j^- , hence changing the quantum label π_o . As discussed previously, the ground state lies in the sector $\pi_o = 0$, thus annihilating any operator that changes π_o . It follows that only the plaquette in the positive direction will contribute non-trivially to the 2-point correlator, and the matrix elements are found to be:

$$\langle \Omega | (A_a^I(v_o)A_b^J(v_o))^G | \Omega \rangle = \frac{1}{2}\delta_{IJ}\langle \Omega | H(\square_{ab}) | \Omega \rangle. \quad (\text{A23})$$

Note that this corresponds to a single plaquette as it appears in the magnetic part of the Hamiltonian (A20) and 2-point correlator; however, it vanishes under different regularizations of the Hamiltonian and on larger lattices. In this manuscript, it nonetheless serves as a well-defined measure for correlations in the system in different directions, while showing that different field species $I = 1, 2, 3$ are completely uncorrelated.

Having those expressions explicitly, one can perform a numerical analysis of the eigen system once a suitable cut-off j_{max} has been introduced. The properties of the system will change when increasing j_{max} , therefore motivating its choice *a posteriori* upon increasing it sufficiently until a certain convergence for the phenomena of interest has been achieved.⁶ Note that interest in different phenomena will require different cut-offs. In fact, analysis involving the ground state performs relatively mild with respect to the choice of j_{max} , as can be shown numerically: in Figure 6 (a) and (b), one can see that $j_{max} = 3/2$ can capture the phase transition from uncorrelated to correlated phase (much more precise than $j_{max} = 1/2$) motivating us in this paper to choose this cut-off, and use as proxy for the accuracy of the *variational quantum eigensolver* (VQE) the difference at each λ to the converged values when $j_{max} \rightarrow \infty$. Only in the strongly correlated regime does the cut-off $j_{max} = 3/2$ fail to capture the behavior with high accuracy. This is expected because the analytic ground state of the system

at $\lambda = 1$ can be written formally as a Dirac- δ -distribution over the group elements associated to each plaquette as

$$\Omega_{\lambda=1}(\vec{h}_\square) = \prod_{\square} \delta(h_\square, e) \quad (\text{A24})$$

as the minimal energy corresponds to the sum of traces over each plaquette, which extremizes at $\text{tr}(e) = 2$. For the Θ -graph, this gives the vacuum energy of $E_{0,\lambda=1} = -12$ exactly, and we see that even at finite cut-off j_{max} the energies rapidly converge towards this value. However, not all features can be caught qualitatively well at these small cut-offs. E.g., we note that if one were interested in other physics such as the energy gap, a cut-off $j_{max} > 2$ is mandatory to see the decrease in energy gap $\Delta = E_1 - E_0$ in the highly correlated regime, which is neither captured by $j_{max} = 1/2$ or $j_{max} = 3/2$, see Figure 6 (c). In fact, higher cut-offs become relevant for the energy gap, as it is known to vanish for pure gauge theories for $\lambda = 1$ because the trace over a plaquette takes on continuous values. Nonetheless, with the tools established in this paper, the regime of $\lambda < 1$ is in principle accessible for VQE methods on sufficiently large and accurate quantum devices using several qubits to store each irrep. We reserve this extension for future work.

Appendix B: Systematic state preparation (SSP) circuits

In this appendix, we first introduce the general strategy to construct quantum circuits for systematic state preparation (SSP) of non-Abelian LGTs and, second, demonstrate this procedure in concrete examples for the lowest lying superselection sector of the 6-valent vertex studied in the main text and in [64].

1. General setup for SSP

The SSP proposed in the main text is based on various developments in recent years to realize ground states of LGTs with shallow quantum circuits, while enriching it with the additional complexity encountered for non-Abelian LGTs. Notably, in contrast to theories such as \mathbb{Z}_2 , the non-Abelian nature renders many methods, including the weight-adjustable loop ansatz (WALA) [12] and mean-field ansätze [18], unsuitable.⁷

We borrow, nevertheless, from WALA the idea of parsing conditional creations of full plaquettes into the state,

⁶ Currently, there is an ongoing effort in the field to determine the possible error due to finite cut-off a priori; however, these methods have not yet matured to apply to non-Abelian gauge theories [56].

⁷ The added complexity comes from the bosonic nature of each link and the multi-fusion rules when coupling plaquettes together, see Section A. The analytic ground state for $\lambda \rightarrow 1$ is no longer the polarized product state, but rather a Dirac distribution peaked over the identity for each Wilson loop in the Hamiltonian, as seen in (A24).

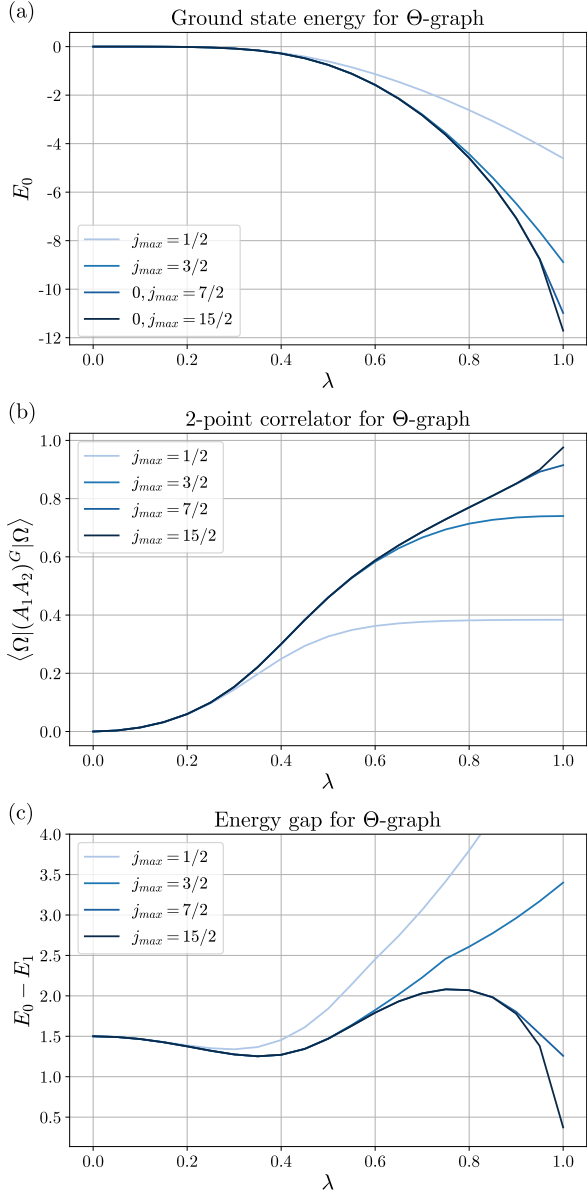


FIG. 6. Numerical analysis of the cut-off dependency for the Θ -graph ($\pi_o = 0$ superselection sector of the single vertex). (a) Ground state energy varied with respect to the coupling parameter λ converges around $j_{max} = 4$. (b) 2-point correlation function indicates a phase transition around $\lambda \approx 0.5$ which is resolved with high accuracy at $j_{max} = 3/2$. (c) The gap to the first excited state has a local minimum around the facsimile phase transition and vanishes for $\lambda \rightarrow 1$ and $j_{max} \rightarrow \infty$.

thereby creating gauge-invariant excitations at all instances, i.e., elements of \mathcal{H}_G . This is beneficial against a dense *hardware-efficient ansatz* (HEA) [27] which samples the whole simulatable Hilbert space \mathcal{H}_S on the quantum computer and suffers from a far larger number of required optimization parameters because in all so-far proposed non-Abelian simulations $\mathcal{H}_G \subset \mathcal{H}_S$. Said simulatable Hilbert space is defined by $\mathcal{H}_{S,n_q} := \otimes_{n_q} \{0, 1\}$

with n_q many qubits and maps to the spin-network functions by assigning qubit registers of $r = \log_2 j_{max}$ qubits to each link e :

$$\mathcal{H}_e = \mathbb{Z}_{2j_{max}} := \{0, \dots, 2j_{max} - 1\} \equiv \mathcal{H}_{S,r}. \quad (\text{B1})$$

Note that we apply the same procedure to each intertwiner label π . However, depending on the valency of the graph, the dimension of the intertwiners may change. In the basis chosen in (A6), we have $\pi_{\pm} \in \mathbb{Z}_{2j_{max}}$, but $\pi_o \in \mathbb{Z}_{3j_{max}}$.⁸ Now, parsing a gauge-invariant excitation, such as a closed curve, onto the quantum state requires a change in all the quantum registers belonging to said curve. Schematically, this is represented in Figure 7 (a) and requires an operation on each register, typically implemented with a common ancilla as in Figure 7 (b) to create a superposition of the gauge-invariant excitation being both applied and not applied. In contrast to \mathbb{Z}_2 , the operation to change the register is not a single CNOT gate, but requires raising/lowering the number represented on the register. I.e., we define the raising/lowering multi-qubit operations A_r^{\pm} on an r -qubit register. Their explicit form depends on the ordering within the register, and we give a concrete example in the following subsection for $r = 2$. The general idea is now to add successively on all minimal plaquettes excitations to the system, which, if concatenated, also distribute excitations among the lattice, as operations of the form $A_{r_4}^+ A_{r_3}^+ A_{r_2}^- A_{r_1}^-$ keep the total number of excitations constant, while flipping strings, see Figure 7 (c). Alternatively, suitable conditional SWAP operations along the lattice may be used to achieve a similar effect. Further, the addition of parametrized phase circuits in between them is necessary to allow for various signs on the states and incurs little additional 2-qubit gate cost. We mention in passing that there is a beneficial procedure to create the initial excitations, which benefit from the knowledge of several registers being in the ground state and therefore come at a reduced 2-qubit gate cost [64]. To parse this procedure onto large systems, an ordering of the circuit has to be chosen, similar to the procedure advocated in [12]. Yet, this ancilla-free procedure works only on the initial excitations. However, as non-Abelian LGT requires the option for arbitrary excitations on each link, the use of additional ancillas cannot be circumvented in general. Lastly, let us mention that the SSP procedure described here has a natural limit in terms of circuit depth, imposed by the cut-off j_{max} in the system: to ensure unitarity of the operations A_r^{\pm} , it cannot always increase the register entry, and most implementations will be chosen such that $A^+ |j_{max}\rangle = |0\rangle$. One must

⁸ A more symmetrical basis would be first coupling the edges in each direction together, i.e., j_k^{\pm} to a common π_k , $k = 1, 2, 3$, and then coupling all π_k on a common 3j-symbol. Here it would be $\pi_k \in \mathbb{Z}_{2j_{max}}$, effectively reducing the required Hilbert space size. However, due to the presence of superselection sectors in the toy model, this manuscript works in the asymmetric intertwiner basis of (A6).

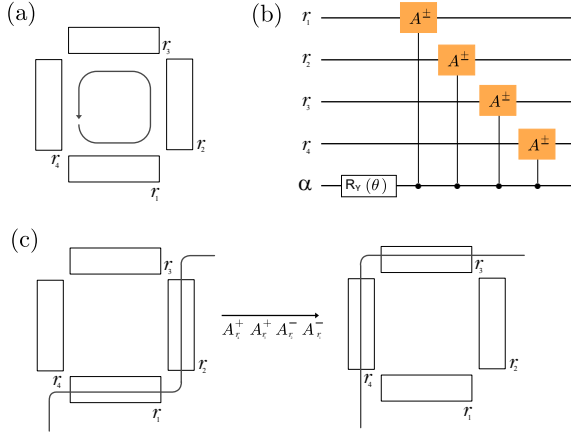


FIG. 7. (a) Graphical representation of gauge-invariant excitations acting on qubit registers r_k forming a minimal plaquette. According to the coupling rules for $SU(2)$, the values in each register will be either raised or lowered. (b) Conditional action of the plaquette operator via a common ancilla qubit α and amplitude θ . Any creation via A^+ conserves the gauge-invariant subspace at least until j_{max} is reached. (c) Any other plaquette can be created via concatenating these operations, e.g., a flip of a string is achieved by $A_{r_4}^+ A_{r_3}^+ A_{r_2}^- A_{r_1}^-$.

therefore either avoid or pay additional attention to circuits that apply more than j_{max} -many raising operations on the same register, see the following subsection.

2. Implementation of SSP on Θ -graph

To illustrate SSP, we note that for the Θ -graph, the minimal plaquettes consist of two edges only, thereby simplifying the excitation creation in terms of actual 2-qubit gate count. With the Hilbert space spanned by the states $|j_1, j_2, j_3\rangle$, which are labeled by the irrep over each of the three edges, we focus here on raising operations. E.g., on the pair 1,2, while leaving edge 3 invariant

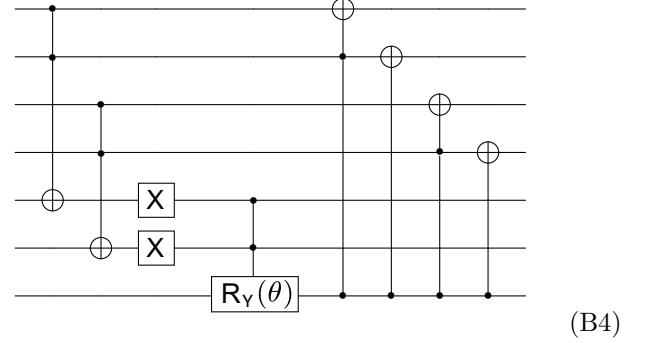
$$j_1 \rightarrow j_1 + \frac{1}{2}, \quad j_2 \rightarrow j_2 + \frac{1}{2}, \quad j_3 \rightarrow j_3. \quad (\text{B2})$$

By restricting to $r = 2$ -qubit registers ($j_{max} = 3/2$) for each edge, we denote the qubits constituting a register as follows: $j_k \equiv (j_{k,1}, j_{k,2})$. Now, we can encode the raising operator as

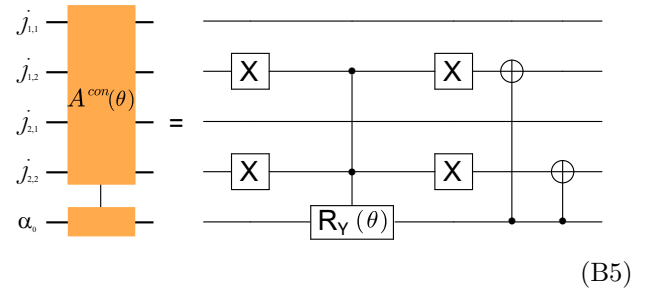
$$\begin{array}{c} \dot{j}_{1,1} \\ \dot{j}_{1,2} \end{array} \begin{array}{|c|} \hline A_2^+ \\ \hline \end{array} = \begin{pmatrix} 0 & 0 & 0 & 1 \\ 1 & 0 & 0 & 0 \\ 0 & 1 & 0 & 0 \\ 0 & 0 & 1 & 0 \end{pmatrix} = \begin{array}{c} \oplus \\ \bullet \\ \text{X} \end{array} \quad (\text{B3})$$

and $A_2^- := (A_2^+)^\dagger$. To ensure unitarity, the state $|11\rangle$ must be mapped onto $|00\rangle$, which has the potential danger of

mapping to a state violating gauge-invariance. One may either ensure in a given state preparation circuit that no j is in the $|3/2\rangle$ state, or incorporate a check whether one of the irreps is in $|3/2\rangle$, i.e., the register being in the $|11\rangle$ state. This check can be accomplished by a Toffoli (CCNOT) gate, controlled by both qubits belonging to a j , which is used on an ancilla qubit. Then the excitation is only allowed if the ancilla qubits for both j_1 and j_2 are $|0\rangle$, which can be checked by using a CCRY gate towards a third ancilla qubit which serves as control for $A_{r_2}^+ A_{r_1}^+$, i.e.:

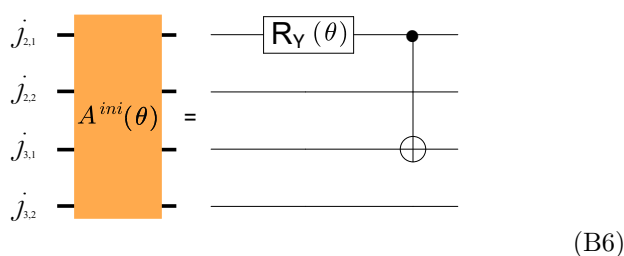


For this, all ancilla qubits must be in the $|0\rangle$ state initially. The first two ancilla qubits can be brought back to $|0\rangle$ afterward using two more Toffoli gates, but the third ancillary qubit can only be reset to $|0\rangle$ by measuring due to its entanglement with the qubit registers created by $CA_{r_2}^+ A_{r_1}^+$. I.e., each such occurrence increases the likelihood of the SSP protocol failing and should therefore be used in moderation. A not-as-general, but cheaper way to add conditional excitations is when checking only the qubits encoding the half-integer digit of both registers. If both are in state $|0\rangle$, then rotating them into $|1\rangle$ always conserves the gauge-invariant subspace. This simplified excitation will be used for the conditional excitation in SSP4 below:



Finally, we note that at the start of each SSP protocol, one knows that the qubits are in $|0\rangle$, which can be utilized to design an initial, cheaper creation of excitations, called in the following A^{ini} , without needing ancilla qubits and

ignoring the higher entries of the qubit registers:



We briefly comment on the 2-qubit gate cost for A_2^+ , which consists of 2 CNOT and 2 Toffoli gates. While the standard decomposition of a Toffoli gate uses 6 CNOT gates (bringing the total 2-qubit gate cost of this block to 14), there is a cheap modification congruent to the Toffoli gate modulo phase shifts [65], in which the state $|101\rangle$ receives a relative phase of -1 , see Figure 8. This decomposition uses only 3 CNOT gates, bringing the 2-qubit gate cost of a modified \tilde{A}_2^+ to 8. In our application, the additional phase is not problematic as it also preserves gauge invariance. In order to increase the fidelity in the presence of noise, we will use this phased decomposition in the following, unless mentioned otherwise.

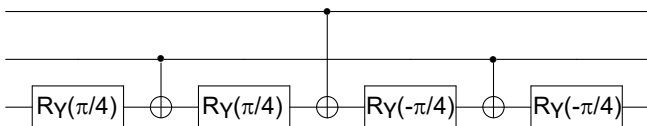
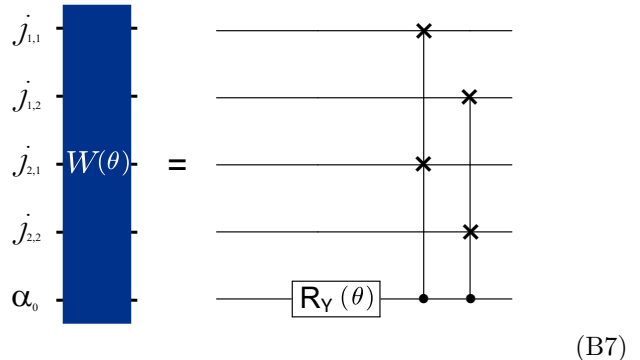


FIG. 8. Cheap decomposition congruent to a Toffoli gate modulo phase shifts (i.e., a phase of -1 on the $|101\rangle$ state).

Additionally, we mention that parameterized changes of the phase of states with respect to each other, which single-qubit gates can achieve, cannot violate gauge invariance and can always be added, due to the Hamiltonian being real and symmetric, its eigenstates will not carry a complex phase. Hence, all single-qubit rotations can be chosen to be parametrized by $R_Y(\theta)$ gates. Further, it is possible to conditionally move excitations around the lattice, thereby generating more symmetric states, which – as outlined in the main text – may prove helpful in generating translationally invariant states. This can be done with a sufficient concatenation of CSWAP gates such that gauge invariance in the final state is preserved. Again, this requirement simplifies in the present Θ -graph, as the swap of just two irreps already presents a gauge-invariance-preserving operation, i.e., when $|j_1 j_2 j_3\rangle$ is a valid state, then $|j_i j_j j_k\rangle$ will also be a valid state for every permutation of $i, j, k \in \{1, 2, 3\}$. Doing such a conditional swap in a parameterized way is done by first rotating an ancilla qubit by an angle θ and then applying CSWAP gates controlled by the ancilla

qubit onto the upper and lower qubit pair:



At the end of the circuit, each ancilla qubit is rotated by a Hadamard gate to create an entangled state, and post-selection ensures that the measured ancilla is in $|0\rangle$. Finally, we provide three explicit constructions based on the above-described rules. These three circuits, SSP2, SSP3, and SSP4, are used in the main text and pump up to 4, 6, 8 excitations, respectively, into the system. At the cost of increasing the 2-qubit gate count and depending on more optimization parameters, higher accuracy can be achieved far into the highly correlated regime. In general, given a cut-off $j_{max} = 3/2$, the upper maximum of gauge-invariant excitations on the Θ -graph would be 8 and hence not every state can be reached by the here expressed circuits. However, even for $\lambda = 1$, we find that SSP4 captures the ground state with high accuracy. For small λ , mainly states with low j values contribute, making the cheaper alternatives, SSP2 and SSP3, viable.

Appendix C: Digital Twin

The simulations performed in Section III B have all been performed on an emulated qubit chip, inspired by contemporary superconducting qubit hardware. The underlying framework is the Qiskit Aer simulator [66, 67] designed for modeling noisy quantum circuits. To incorporate the constraints originating from finite connectivity, we assume a square lattice topology to embed the up to 8 qubits for the SSP circuits. In particular, the 17-qubit and 24-coupler chip architecture presented in Figure 10 was used. The coupling map is passed to the built-in Qiskit transpiler at optimization level 3 to obtain an executable circuit that meets the minimum requirements with respect to swap operations. To make the noise model more in line with realistic hardware, we allowed only for CZ gates as the native 2-qubit gate, which can be implemented on superconducting qubit hardware with tunable couplers [68]. The characteristic noise profiles of all native gates were numerically simulated and passed as Kraus operators to the Qiskit Aer simulator, replacing the naive coherence-based noise maps. In numerical simulations, it was found that the Kraus operator corresponding to the gate in [68] features both systematic and stochastic errors, with systematic profiles

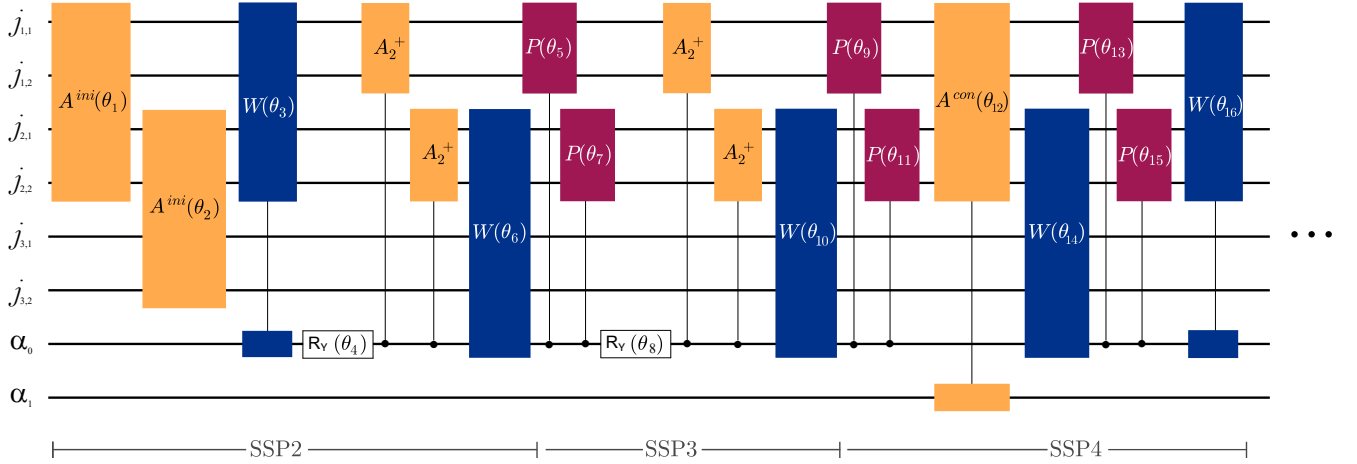


FIG. 9. The full systematic state preparation protocol, which successively adds further excitations to the Θ -graph. Cutting the circuit at various stages gives rise to the various SSP2, SSP3, and SSP4 used in the main text. Next to the excitation and swap operations defined in the main text, the circuit also features phase gates P , which are a concatenation of an $R_Y(\theta)$ and a CZ gate.

dominating. This is, in fact, advantageous for the VQE algorithm in the main text, as the optimization parameters in the circuits will be able to mitigate systematic shifts by adapting the optimization parameters. This built-in error mitigation is one of the reasons why applications based on VQE hold promise, even for the current *noisy-intermediate scale quantum* (NISQ) era and

the mid-sized quantum devices available at present. To be in agreement with the current achievable fidelities as those by *IBM Quantum*, e.g. Heron R2 [69], and *Google Quantum*, e.g. Willow [70], we fixed the values in the main text of this manuscript to 2-qubit gate error of 0.5% and single qubit error of 0.05%.

In Figure 11, we present exemplary results from VQE runs on this digital twin with different SSP variants.

Appendix D: Comparison with HEA

The SSP utilizes knowledge of the system in question by only creating gauge-invariant states and therefore scaling mildly in optimization parameter count. On the other hand, the HEA relies only on a multitude of optimization parameters to sample a large part of the total Hilbert space and therefore achieves high expressibility while remaining agnostic to the system in question. The fact that HEA is more dense and has a lower 2-qubit gate count than SSP raises the expectation that it may perform better in the NISQ area, while – once qubit errors become suppressed – it is in danger of running into the barren plateau problem [25, 46–48]. In the following, we will investigate the impact of additional optimization parameters on the scaling in terms of additional cost-function evaluations associated with a vanishing gradient.

There are slight variants of HEA used in the literature, see [71] for a list of contemporary proposals. We focus in this paper on the architecture depicted in Figure 1 (a),

as relevant differences in their performance are not expected at the small system size considered in the present 6-valent vertex model. As both HEA and SSP are families of algorithms parametrized by their depth, we will in our analysis compare different variants of SSP and HEA *a posteriori* depending on the accuracy they could reach in ideal (i.e., noise-free) simulations⁹. In Figure 12, we show how accurate the algorithms are in preparing a state close to the exact ground state of the 6-valent vertex model at $j_{max} = 3/2$ cut-off. This quantity is not obtainable in real simulations without an extensive quantum state tomography, but is easily obtainable on the digital twin emulator from Section C utilized in this work. For small values of λ , all algorithms reach good approximations to the ground state, while in the regime of large

⁹ This is the limit we are interested in, as the ongoing improvements in qubit gate fidelity spark the hope that quantum devices in the late NISQ era will soon be able to deal with sufficiently deep algorithms when the barren plateau problem can become relevant.

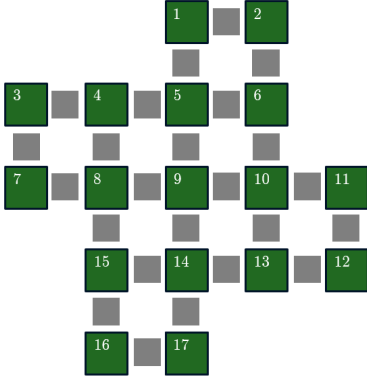


FIG. 10. Layout of the chip with 17 qubits (green) and 24 couplers (grey) onto which the algorithms used in this manuscript have been transpiled for simulation.

λ , deeper algorithms perform better. Comparing different instances of HEA and SSP in terms of their accuracy at $\lambda = 1$ suggests primarily comparing the tuples (HEA18, SSP2), (HEA24, SSP3), and (HEA30, SSP4) as the elements in each of these sets perform similarly. We present a detailed comparison between the two families in Table I with respect to their relevant metrics, such as qubit gate and optimization parameter counts. As expected, the number 2-qubit gates required for SSP is approximately a factor 5 larger than for HEA, while the requirement for optimization parameters is approximately cut in half for the same accuracy level. For the optimizer, we considered two options: one method that utilizes the Hessian (BFGS) and another method based on gradients (Powell). BFGS uses fewer function evaluations than Powell, presumably due to the quicker convergence of using a Hessian. However, when noise is added to the simulation, BFGS does not reliably converge. This is assumed to be due to the Hessian being strongly impacted by faulty measurements. Powell was selected for our calculations regardless of noise presence for consistency. To get a rough idea how the increased optimization parameter count will be reflected in experiments, we study the convergence behaviour of the algorithms in terms of cost-function evaluations: In Figure 13 we show how long it took for algorithms with a given candidate count of $N = 200$ until all candidates reached their local minimum, irrespective of how precise the result was. One can see that the number of required function evaluations increases non-linearly with parameter count. This feature is especially pronounced at $\lambda \approx 0.4$ where the facsimile phase-transition of the system happens. Due to this scaling of needed function evaluations, SSP requires far fewer function evaluations than HEA to reach a similar accuracy. The increase in function evaluations hints at an eventual vanishing of gradients and indicates that the wall-clock time of VQE with HEA in LGT will scale unfavorably, encountering the barren plateau problem, which motivates the use of SSP in future applications.

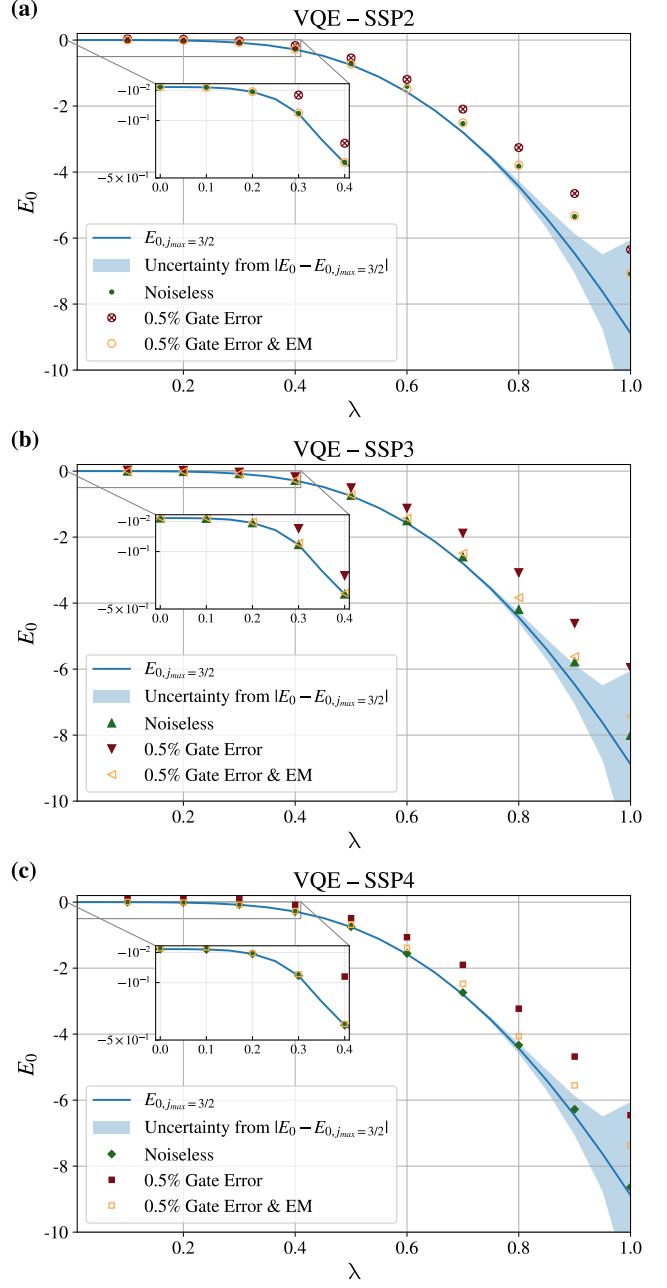


FIG. 11. Best achieved minima for the energy expectation values for various SSP circuits. The VQE has been emulated in an ideal environment (green) and in the presence of noise from a 0.5% 2-qubit gate error (red). Upon adding error mitigation (EM) protocols (orange), the accuracy comes close to the exact energies (blue) and falls within the uncertainty given by the finite cut-off $j_{max} = 3/2$ (shaded region).

Appendix E: Error Mitigation by Symmetry Verification

In this appendix, we discuss the methods of error mitigation (EM) used for the simulation of the VQE algorithm on the digital twin in order to improve the noisy

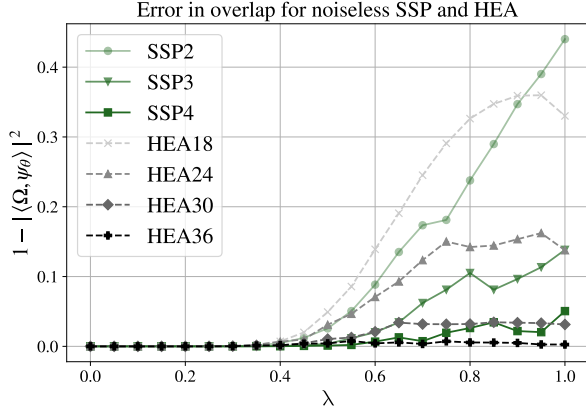


FIG. 12. Comparison of different ansätze with respect to the optimal values reached in the ideal setting. The mismatch with the actual ground state Ω is captured in the error $1 - |\langle \Omega, \psi_{\theta^*} \rangle|^2$. For ansätze reaching the same accuracy, SSP requires fewer optimization parameters than HEA.

qubit gate operations. There is already an extensive body of literature on EM schemes; see [72] for modern implementations. As we only added emulated noise to the system here, we refrain from applying all known error-mitigation schemes to the algorithm and keep those for later implementation.¹⁰ We are focusing on EM schemes that are either post-processing (PP), not as commonly employed or at least need additional input to work for non-Abelian lattice gauge theories.

To see the impact of the EM schemes that we use, we show in Figure 15 how various combinations affect the results of emulating VQE on the 6-valent vertex model with the SSP4 algorithm emulated on the digital twin from Section C. We show the derivation Δ from the expectation value for parameters $\theta^* = \theta^*(EM)$ obtained with various EM methods to exact ground state energy $E_{0, j_{max}=3/2}$ computed at finite cut-off $j_{max} = 3/2$, i.e.¹¹

$$\Delta = \langle \psi_{\theta^*} | H | \psi_{\theta^*} \rangle - E_{0, j_{max}=3/2} \quad (\text{E1})$$

To account for the spread of the result over many samples after optimization, we repeat the readout for $N = 1.000$ samples and plot as solid points the median of the distribution and use error bars to indicate the standard deviation centered around the mean. The

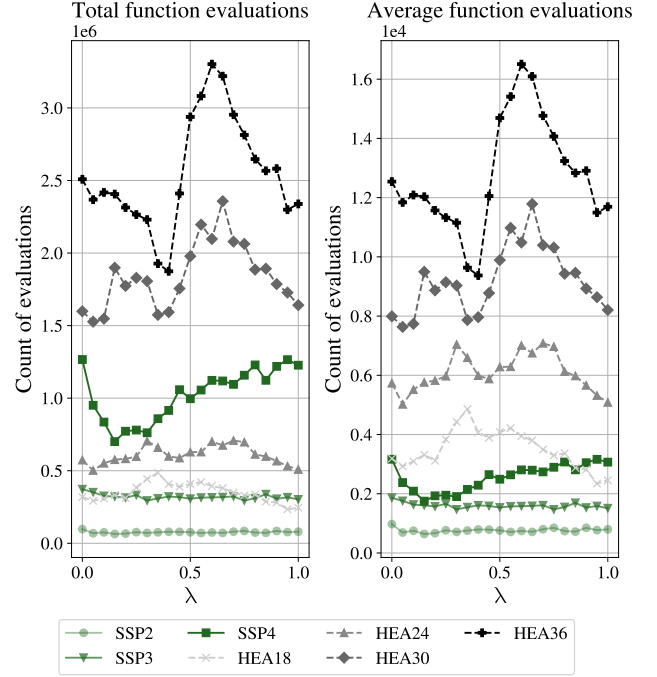


FIG. 13. Number of required evaluations of the cost functions (i.e., measuring the expectation value for the Hamiltonian) for different ansätze. (Left) The total function evaluations count the number of candidates randomly scattered over the parameter landscape. The number of candidates is based on heuristic estimates and does not represent lower bounds. (Right) Average calls of the function evaluation for a single candidate to converge to its local minima.

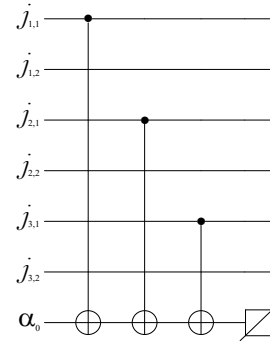


FIG. 14. EM circuit used to perform in-bulk symmetry verification by enforcing condition (7).

following EM methods have been investigated:

o) Complex phase rotation. The ideal circuit profited from knowledge that, in pure $SU(2)$ Yang-Mills theory, the Hamiltonian is real and symmetric, therefore no complex phases appear in the eigenstate, and the state preparation protocol benefited from the possibility to choose always only $R_Y(\theta)$ gates. However, in a noisy environment, dephasing occurs, introducing unwanted complex

¹⁰ Having these tools (such as, e.g., zero-noise-extrapolation, operator density renormalization [72]) in backhand will prove valuable to raise qubit performance on actual hardware.

¹¹ Note, that the Hamiltonian in the spin-network basis projects unphysical states to zero, hence yielding potentially a contribution to (E1). In general, adding a penalty term of sufficient weight on these terms can counteract the impact of any unphysical terms created by noise. In the toy model investigated here, the energy expectation values of the unphysical states in the electric part have been sufficiently shifted upwards.

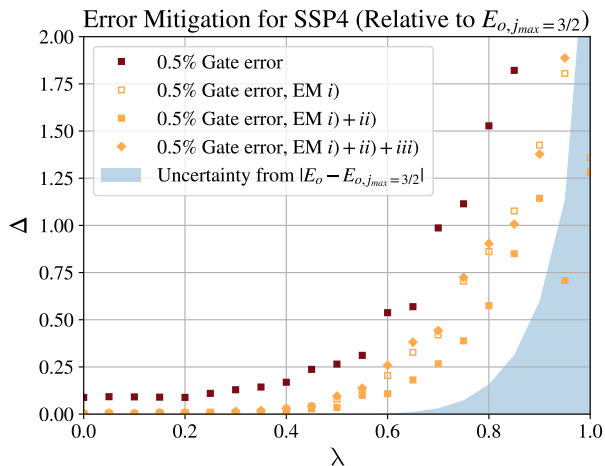


FIG. 15. Effectiveness of various EM schemes exemplified on the error Δ for SSP4. Untreated noisy emulated data (2-qubit gate error $e = 0.005$), shown in red, demonstrate an increase of the error for larger λ values. Applying various EM methods allows for decreasing the error by obtaining better minima. Lastly, to reduce the spread in the results, we remove obvious outliers. This combination of methods *i) – iii)* is used in the main text. Solid points indicate the median, and error bars indicate the standard deviation centered around the mean. In the main text of the manuscript, the used error-mitigation methods are *i) + ii)*.

phases into the prepared state, which cannot be mitigated by parametrized R_Y gates. To only minimally increase the optimization parameters, we will – instead of adding to every R_Y gate an accompanying R_Z gate – only minimally account for the dephasing and set at the end of the circuit the final single qubit rotations to $R_Z(\theta)$ gates. These parameters help mitigate any systematics from dephasing errors in the noise, while in the ideal setting, these gates will always insert phases of only ± 1 . For this reason, we incorporate these complex phases into each circuit and have this EM technique automatically included in all ideal and noisy emulations.

i) PP symmetry verification for gauge-invariance. In the seminal paper on symmetry verification for EM [73, 74], it was advocated to use the presence of symmetries of the system for both in-bulk and PP protocols.¹² We focus first on the latter and note that gauge-invariance also presents a symmetry which is easy to verify by measuring a bit-string and asking whether it obeys the conditions (7) and (8). By performing this check at the end of the circuit, it comes for free without introducing additional noise; however, it is limited in its capabilities to mitigate multiple errors during state preparation or errors that map within the gauge-invariant subspace.

ii) PP rotation symmetry projector. In general, any symmetry of a system may be used as a projection operator in PP. Given that the vacuum in LGT has translational symmetries (which have already been reduced in our toy model) and rotational symmetries by 90 degrees, the latter present a further possibility for applying symmetry verification. Yet, one needs to use caution, as already emphasized in [74], because if a state preparation ansatz breaks the symmetry in intermediate steps, it is prone to introducing biases and needs to be carefully checked. For SSP, a rotation around axis 3 will effectively switch $j_1 \leftrightarrow j_2$ in the ground state; however, the incremental generation of excitations breaks this symmetry. However, due to the symmetrization of the state added during each SSP, the symmetry verification tool can still be used if one confirms *a posteriori* that the cost function gets further minimized by applying this protocol. In our case, we do PP with respect to the following project, symmetrizing $j_1 \leftrightarrow j_2$:

$$P_{12} = (1 + S_{12})/2, \quad S_{12} = \frac{1}{4} \sum_{P,Q \in \{I,X,Y,Z\}} P_1 Q_2 P_3 Q_4 I_5 I_6,$$

with S_{12} the SWAP of qubit registers 1 and 2, while leaving register 3 invariant. The price to pay is that the obtained ground state has a bias towards this symmetry. Hence, expectation values of operators not obeying this symmetry will, in general, be faulty. For the application of this paper, we are interested in the 2-point correlator (A22), which exists for any pair a, b and is on the vacuum independent of this choice. Hence, we can use $P_{1 \leftrightarrow 2}$ if we restrict our analysis to $\langle \Omega | (A_1^I A_2^J)^G | \Omega \rangle$, which has been done in the main text to produce Figure 5.

iii) In-bulk symmetry verification. Lastly, we mention a part of the standard tool-set for symmetry verification [73, 74], namely in-bulk symmetry verification measures. Here, one checks that a certain symmetry in the system is still preserved during the algorithm – often by measurement – and throws away runs where the measurement violates the condition. This procedure must be used in moderation, as successive applications will reduce the number of valid measurements and thus increase the wall-clock time for any algorithm. We use a check of the remaining $3j$ conditions to identify single qubit errors that map out of the gauge-invariant Hilbert space. Explicitly, equation (7) can be verified by checking the one qubit in each register that labels the half-integer value. A successive application of CNOT gates onto an ancilla qubit, as depicted in Figure 14, achieves that, and a run remains valid if the ancilla is measured in $|1\rangle$. However, we mark that this procedure introduces additional 2-qubit gates and therefore a potential further error source. It requires, therefore, a sufficiently good error rate to improve the overall error instead of worsening it. For the contemporary error sources emulated in this article, we simulated in Figure 15 the insertion of a single in-bulk symmetry verification check in the middle of algorithm SSP4 (i.e., at the depth of the circuit corresponding roughly to the end of SSP3, compare Figure 9).

¹² That these tools translate straightforwardly to non-Abelian LGT was already observed in [75].

One can observe that, for the assumed error, the mitigation does not improve the measurement results. We thus

refrain from using this method at the present stage for the error mitigation done in the main text.

Circuit	# Ancillas	# 1-Q Gates	# 2-Q Gates	# Layer	# Opt. Param.	# Cand.	# Avg. Eval.	Error (ideal)
SSP2	1	216	34	90	6	100	793	< 0.45
SSP3	1	394	73	185	10	200	1,608	< 0.14
SSP4	2	524	104	254	16	400	2,289	< 0.06
HEA18	0	104	10	24	18	100	4,074	< 0.34
HEA24	0	142	15	33	24	100	5,989	< 0.14
HEA30	0	180	20	42	30	200	7,963	<0.04
HEA36	0	218	25	51	36	200	9,371	< 0.003
HEA42	0	256	30	60	42	400	12,423	< 0.001

TABLE I. Comparison of requirements for various circuit architectures and their projected (ideal) performance for the single vertex graph, which requires 6 data qubits to store all information for $j_{max} = 3/2$. The systematic state preparation (SSP) circuits are found to require higher qubit-gate count and more layers than circuits using the hardware efficient ansatz (HEA); however, they demonstrate a far tamer scaling in terms of optimization parameters, candidates, and evaluations of the cost function to reach similar ideal accuracy. This translates to a fast convergence of the optimizer and, therefore, alleviates the barren plateau problem. Comparisons of their performance are shown in Figure 12 and Figure 13.